

*Supporting Information for:*

**Probing active site chemistry with differently charged Au<sub>25</sub><sup>q</sup> nanoclusters (*q* = -1, 0, +1)**

Douglas R. Kauffman,<sup>1,\*</sup> Dominic Alfonso,<sup>1</sup> Christopher Matranga,<sup>1</sup> Paul Ohodnicki,<sup>1</sup>

Xingyi Deng,<sup>1,2</sup> Rajan C. Siva,<sup>1</sup> Chenjie Zeng<sup>3</sup> and Rongchao Jin<sup>3</sup>

<sup>1</sup> National Energy Technology Laboratory, United States Department of Energy, Pittsburgh, Pennsylvania, 15236, USA

<sup>2</sup> URS, P.O. Box 618, South Park, Pennsylvania, 15129, USA

<sup>3</sup> Department of Chemistry, Carnegie Mellon University, Pittsburgh, Pennsylvania, 15213, USA

\* Email: Douglas.Kauffman@NETL.DOE.GOV

## Table of Contents

Page

---

<b>Experimental and Computational Methods</b> .....	S3-S6
<b>Figure S1</b> Au <sub>25</sub> <sup>q</sup> crystal structure.....	S7
<b>Figure S2</b> X-ray photoelectron spectra of CB-supported Au <sub>25</sub> <sup>q</sup> clusters.....	S8
<b>Figure S3</b> Optical absorbance of Au <sub>25</sub> <sup>q</sup> before and after electrocatalytic reactions.....	S9-S10
<b>Figure S4</b> Optical absorbance of Au <sub>25</sub> <sup>-</sup> in N <sub>2</sub> purged and CO saturated DMF.....	S11
<b>Figure S5</b> OH stripping charge vs. moles of Au <sub>25</sub> <sup>q</sup> on the electrode surface.....	S12
<b>Figure S6</b> Electrocatalytic current density vs. Au <sub>25</sub> <sup>q</sup> loading.....	S13-S14
<b>Figure S7</b> CO <sub>2</sub> onset and Tafel slope determination, replicate polarization curves.....	S15-S16
<b>Figure S8</b> CO <sub>2</sub> reduction product analysis.....	S17-S18
<b>Figure S9</b> Electrocatalytic activity of the CB-support.....	S19
<b>Figure S10</b> CO <sub>2</sub> + H <sup>+</sup> coadsorption at Au <sub>25</sub> <sup>q</sup> .....	S20
<b>Figure S11</b> Singly-bound CO <sub>2</sub> -Au <sub>25</sub> <sup>q</sup> models.....	S21
<b>Figure S12</b> CO oxidation at various rotation rates and average CO oxidation activity.....	S22-S23
<b>Figure S13</b> CO + OH <sup>-</sup> coadsorption at Au <sub>25</sub> <sup>q</sup> .....	S24
<b>Figure S14</b> Singly-bound CO-Au <sub>25</sub> <sup>q</sup> models.....	S25
<b>Figure S15</b> OH <sup>-</sup> binding energies at Au <sub>25</sub> <sup>q</sup> .....	S26
<b>Figure S16</b> Electrochemical O <sub>2</sub> reduction at Au <sub>25</sub> <sup>q</sup> .....	S27-S28
<b>Table S1</b> Adsorbate binding energies.....	S29
<b>Table S2</b> OH <sup>-</sup> stripping potentials.....	S30
<b>Equations S1-S5</b> CO <sub>2</sub> reduction.....	S16
<b>Equations S6-S8</b> CO oxidation.....	S22
<b>Equations S9 and S10</b> O <sub>2</sub> reduction.....	S27
<b>References</b> .....	S31-S32

## Experimental and Computational Methods

**General.** Au<sub>25</sub><sup>-</sup> clusters capped with phenylethylthiol (-SCH<sub>2</sub>CH<sub>2</sub>Ph) ligands were synthesized according to previously published methods.<sup>1</sup> All aqueous solutions were prepared with certified ACS grade KOH or KHCO<sub>3</sub> (Fisher Scientific) and deionized water purified through a Barnstead Easypure II water purification system (Thermo Scientific). Spectroscopic grade dimethylformamide (DMF; 99.8%, Acros Organics) was dried over molecular sieves prior to use. All gases were ultra-high purity (UHP) grade.

**Isolation of particular Au<sub>25</sub><sup>q</sup> charge states.** Different Au<sub>25</sub><sup>q</sup> charge states were isolated according to our previously published method.<sup>2</sup> Au<sub>25</sub>(PET)<sub>18</sub><sup>-</sup> was dissolved in N<sub>2</sub> purged DMF and transferred into a sealable, septum-capped cuvette. The cuvette was wrapped with Al foil to exclude ambient light and the solution was purged with N<sub>2</sub> for 30 minutes. Excluding ambient light during this initial step is important because O<sub>2</sub> can photo-oxidize Au<sub>25</sub><sup>-</sup> into Au<sub>25</sub><sup>0</sup>.<sup>2</sup> UV-Vis absorbance spectra of Au<sub>25</sub><sup>-</sup> were then collected on an Agilent 8453 photodiode array spectrophotometer. Au<sub>25</sub><sup>0</sup> was isolated by bubbling the solution with O<sub>2</sub> for 1 hour while the solution was illuminated with a 350 W Xe-arc lamp through a 650 nm long-pass optical filter (hν ≤ 1.9 eV). The light contained energy greater than the Au<sub>25</sub><sup>q</sup> HOMO-LUMO energy gap of ~1.4 eV and it promoted excited state Au<sub>25</sub><sup>q</sup>-O<sub>2</sub> charge transfer.<sup>2</sup> Light containing less energy than the Au<sub>25</sub><sup>q</sup> HOMO-LUMO gap does not initiate excited-state charge transfer. UV-Vis spectroscopy confirmed the isolation of Au<sub>25</sub><sup>0</sup> (see ref. 2 and figure 1c in the main text). This is a one electron process that stops after Au<sub>25</sub><sup>0</sup> formation. Au<sub>25</sub><sup>+</sup> was isolated by adding ~10-20 molar excess of tetrabutylammonium perchlorate (TBAP) and bubbling O<sub>2</sub> through a Au<sub>25</sub><sup>-</sup> or Au<sub>25</sub><sup>0</sup> solution during illumination with λ ≥ 650 nm light. The perchlorate anion stabilized Au<sub>25</sub><sup>+</sup> while the TBA<sup>+</sup> cation stabilized O<sub>2</sub><sup>-</sup>. This process stopped after Au<sub>25</sub><sup>+</sup> formation and UV-Vis spectroscopy confirmed the isolation of Au<sub>25</sub><sup>+</sup>. The Au<sub>25</sub><sup>0</sup> or Au<sub>25</sub><sup>+</sup> absorbance spectra stabilized after ~20-30 minutes of illumination. However, a one hour illumination period was used to ensure complete charge state conversion.

**Precipitation onto the Carbon Black Support.** Particular Au<sub>25</sub><sup>q</sup> charge states were isolated in DMF as described above. They were then sonicated with Vulcan XC-72R carbon black (CB) in the absence of light. The PET-capped Au<sub>25</sub><sup>q</sup> are not soluble in methanol (MeOH), and MeOH addition precipitated the Au<sub>25</sub><sup>q</sup> clusters onto the CB support. The Au<sub>25</sub><sup>q</sup>/CB suspension was centrifuged and the liquid was decanted off. The CB-supported Au<sub>25</sub><sup>q</sup> clusters were re-sonicated in fresh MeOH, centrifuged again and the MeOH was decanted off. This was done a total of 3 times. Samples were then dried under N<sub>2</sub> for future use. The ratio of Au<sub>25</sub><sup>q</sup> to CB was adjusted through the starting concentration of Au<sub>25</sub><sup>q</sup> in DMF and the volume of dissolved Au<sub>25</sub><sup>q</sup> added to CB.

**Electron Microscopy.** Transmission electron microscopy (TEM) was performed using a Tecnai F20 field emission microscope operating at 200kV. Images were collected in STEM mode using a high angle annular dark field (HAADF) detector for z-contrast imaging. Sample preparation

was performed by sonicating CB-supported Au<sub>25</sub><sup>q</sup> in methanol and depositing ~10  $\mu$ L onto a 50 nm thick Si<sub>3</sub>N<sub>4</sub> membrane grid (Ted Pella). Caution was taken to use the lowest possible electron dosage that provided adequate contrast for imaging and subsequent particle size analysis. This experimental setup was used to avoid damaging the particles during imaging. We did not observe particle sintering or other morphological changes during TEM imaging.

**X-ray Photoelectron Spectroscopy (XPS).** XPS experiments were carried out in a commercial UHV chamber from Omicron Nanotechnology GmbH with a base pressure of  $\sim 3 \times 10^{-10}$  mbar. The Au 4f spectra of the CB-supported Au<sub>25</sub><sup>q</sup> samples were collected using an MgK $\alpha$  X-ray source (DAR 400, 1253.6 eV, 75 W) and a hemispherical electron spectrometer (SPHERA Energy Analyzer) with pass energy of 20 eV at room temperature. The binding energy of the CB-supported Au<sub>25</sub><sup>q</sup> samples was calibrated to the Au 4f<sub>7/2</sub> peak of a clean single crystal Au(111) at 83.8 eV.

**Electrochemistry.** CB-supported Au<sub>25</sub><sup>q</sup> clusters were sonicated in a mixture of 200  $\mu$ L methanol and 20  $\mu$ L of a 5% Nafion solution. 5-20  $\mu$ L of the Au<sub>25</sub><sup>q</sup>/CB suspension was then dropcast onto a glassy carbon electrode. The Nafion binder adheres the CB-supported Au<sub>25</sub><sup>q</sup> to the electrode but still allows solvent and reactant access to the cluster surface. Electrochemical experiments were conducted with a Biologic SP-150 potentiostat and a Pine Instruments electrode rotation controller. Cyclic voltammetry (CV) was repeated until stable curves were obtained. Polarization curves were then taken from the stabilized CVs. A Hydroflex reversible hydrogen electrode (abbreviated RHE, from eDAQ) was used for CO<sub>2</sub> reduction studies. A Ag/AgCl (3.0 M NaCl, from BASi) reference electrode was used for CO oxidation and O<sub>2</sub> reduction studies. The Ag/AgCl electrode was calibrated against the RHE in N<sub>2</sub> purged 0.1M KOH after each experiment, and all potentials are reported in the RHE scale. A Pt wire counter electrode was used for CO<sub>2</sub> and O<sub>2</sub> reduction experiments. A Au wire counter electrode was used for CO oxidation reactions.<sup>3</sup>

**Quantification of Au<sub>25</sub><sup>q</sup> on the Electrode Surface.** OH stripping voltammetry was conducted in N<sub>2</sub> purged 0.1 M KOH. Au<sub>25</sub><sup>-</sup> was first dissolved in acetone and the absorbance spectrum was collected. The concentration of the Au<sub>25</sub><sup>-</sup> solution was determined from the known molar absorptivity [ $\epsilon = 8.8 \times 10^3$  a.u./M/cm @ 1.83 eV (680 nm, labeled peak *a* in figure 1c of the main text)].<sup>4</sup> A precise volume of dissolved Au<sub>25</sub><sup>-</sup> (in acetone) was added to 200  $\mu$ L of CB suspended in MeOH (1 mg/mL in MeOH). Additional MeOH was then added to bring the mixture volume to 300  $\mu$ L. The mixture was briefly sonicated and 20  $\mu$ L of Nafion was added to bring the total solution volume to 320  $\mu$ L. The mixture was briefly sonicated once more and then the Au<sub>25</sub><sup>-</sup>/CB mixture was added to a GC electrode in 5.5  $\mu$ L increments. Total Au<sub>25</sub><sup>-</sup>/CB loadings on the electrode ranged between 5.5-11  $\mu$ L (1-2 additions). Cyclic voltammetry was conducted at  $\omega = 2500$  RPM between +0.44 and +1.94 V vs. RHE until stable OH<sup>-</sup> stripping voltammograms were obtained. The OH stripping peak was then integrated and plotted against the moles of Au<sub>25</sub><sup>-</sup> on the electrode surface (figure S5). Alternatively, the electrochemical surface area (ECSA) could

be estimated from the OH stripping peak area using the literature value for bulk Au ( $390 \mu\text{C cm}^{-2}_{\text{Au}}$ ).<sup>5</sup>

**Turnover Frequency Determination.** Turnover frequencies (TOF: molecules/ $\text{Au}_{25}^q/\text{s}$ ) were determined from the polarization curves using the current density ( $\text{A/mol Au}_{25}^q$ ), Faraday's constant ( $96485 \text{ C/mole e}^-$ ), and the experimentally determined number of electrons transferred in the reaction ( $n = 2e^-$  for  $\text{CO}_2$  reduction and CO oxidation, and  $n = 3e^-$  for  $\text{O}_2$  reduction).<sup>6</sup> Electron transfer numbers were determined by analysis of  $\text{CO}_2$  reduction products or Levich analysis of the CO and  $\text{O}_2$  RDE polarization curves (see figures S12 and S16). An example TOF calculation is provided below.

$$\text{TOF} = \frac{\text{current density "j" } \left( \frac{\text{A}}{\text{mole Au}_{25}^q} \right)}{\left( 96485 \frac{\text{C}}{\text{mole e}^-} \right) \left( \frac{\text{A} \cdot \text{s}}{\text{C}} \right) \left( \frac{2 \text{ e}^-}{\text{molecule}} \right)}$$

**Example:**  $\text{Au}_{25}^-$  produced a  $\text{CO}_2$  reduction current density of  $1.84 \pm 0.11 \times 10^7 \text{ A/mole}$  at  $-1\text{V}$ . This provides a TOF of  $95 \pm 6$  molecules/ $\text{Au}_{25}^-/\text{s}$ .

**$\text{CO}_2$  reduction product analysis.**  $\text{CO}_2$  electrolysis experiments were conducted in a sealed, two compartment H-cell at  $-1 \text{ V vs. RHE}$  (figure S8). One compartment contained a stationary glassy carbon working electrode and a Ag/AgCl reference electrode; the Ag/AgCl electrode was calibrated against the RHE in  $\text{CO}_2$  saturated  $0.1\text{M KHCO}_3$  prior to each electrolysis run. The other half of the H-cell contained a Pt wire counter electrode. A  $0.1778 \text{ mm}$  ( $0.007 \text{ inch}$ ) thick Nafion 117 cation exchange membrane separated the two chambers. This setup prevents  $\text{CO}_2$  reduction products from escaping the working electrode chamber, but allows current to flow *via* proton conduction through the Nafion membrane. After one hour of electrolysis the products were analyzed with a Perkin Elmer Clarus 600 gas chromatograph. Faradaic Efficiencies (FE) were calculated from the integrated reaction charge and the detected reaction products.

**Computational Methods.** All calculations reported in this work were done with spin-polarized density functional theory (DFT) implemented in the VASP code.<sup>7</sup> This implementation includes total energy and atomic force calculations. Plane-wave basis sets with a cutoff energy of  $600 \text{ eV}$  were used to expand the Kohn-Sham one-electron valence states. The generalized gradient approximation (GGA) using the Perdew-Burke-Enzerhoff (PBE) functional was employed to calculate the exchange-correlation energy.<sup>8</sup> The interactions of the valence electrons with the core electrons and the nuclei were described by the projector-augmented wave (PAW) all-electron potentials within the frozen-core approximation.<sup>9</sup>

The fully ligand-protected  $\text{Au}_{25}(\text{SCH}_3)_{18}^q$  clusters were based on the published  $\text{Au}_{25}(\text{SR})_{18}^-$  crystal structure<sup>1</sup> and a previously DFT-optimized model.<sup>10</sup> Following our previous work,<sup>11</sup> a  $\text{Au}_{25}$  core capped with 18  $-\text{SCH}_3$  ligands was used to construct a model for the  $\text{Au}_{25}(\text{SCH}_3)_{18}^-$  cluster. It was placed in a cubic box of  $a = 24 \text{ \AA}$  to ensure the decoupling of periodic images and a uniform compensating background charge was assumed. Models for

$\text{Au}_{25}(\text{SCH}_3)_{18}^0$  and  $\text{Au}_{25}(\text{SCH}_3)_{18}^+$  clusters were built by removal of one and two electrons from this structure. Geometry optimization of adsorbates on the  $\text{Au}_{25}(\text{SCH}_3)_{18}^q$  clusters was carried out using a quasi-Newton variable metric algorithm until the total force on the atoms was less than  $0.03 \text{ eV}/\text{\AA}$ . A  $\Gamma$ -point sampling of the Brillouin zone was utilized in the calculations of the ground state. For Au, S, C, and O we used the standard PAW potentials acting on eleven ( $5d^{10}$  and  $6s^1$ ), six ( $3s^2$  and  $3p^4$ ), four ( $2s^2$  and  $2p^2$ ) and six ( $2s^2$  and  $2p^4$ ) outer core/valence electrons, respectively. A Gaussian smearing of  $\sigma = 0.2 \text{ eV}$  was used and the corrected energy for  $\sigma \rightarrow 0$  was employed. The binding energy was computed using the expression  $E_{\text{ads}} = E_{\text{adsorbates+cluster}} - (E_{\text{adsorbate}} + E_{\text{cluster}})$ .  $E_{\text{adsorbates+cluster}}$  is the total energy of the relaxed adsorbates-cluster system.  $E_{\text{cluster}}$  and  $E_{\text{adsorbate}}$  are the total energy of the relaxed bare cluster and free adsorbates, *i.e.* the adsorbates as stable molecules or radicals in the gas phase.

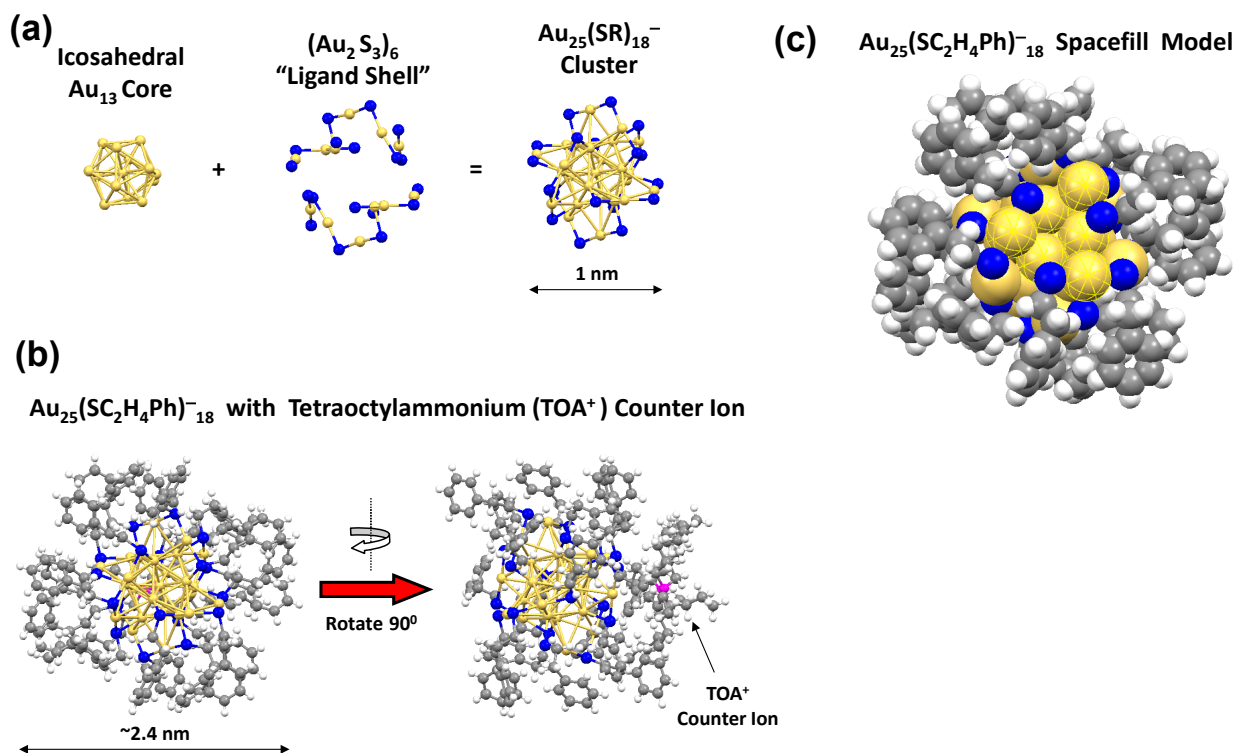


**Figure S1.** Components of the  $\text{Au}_{25}(\text{SCH}_2\text{CH}_2\text{Ph})_{18}^- \text{TOA}^+$  crystal structure. Images were created from the crystallographic information files published in references 1a and 1b. The clusters are abbreviated as  $\text{Au}_{25}^q$  ( $q = -1, 0, +1$ ) in this manuscript. (a) The  $\text{Au}_{25}^q$  cluster contains an  $\text{Au}_{13}$  "core" surrounded by a "ligand shell" with six  $(\text{Au}_2\text{S}_3)$  semi-ring structures. (b) Organic phenylethylthiol (PET) ligands extend off the S atoms in the ligand shell.  $\text{Au}_{25}^-$  is stabilized by a positive tetraoctylammonium ( $\text{TOA}^+$ ) counter ion. The cluster is approximately 1 nm in diameter excluding the organic ligands and  $\sim 2.4$  nm including the organic PET ligands. (c) A space fill model of the  $\text{Au}_{25}^q$  cluster. The cluster's molecular adsorption "pocket" is highlighted with yellow cross-hatches.<sup>11</sup>

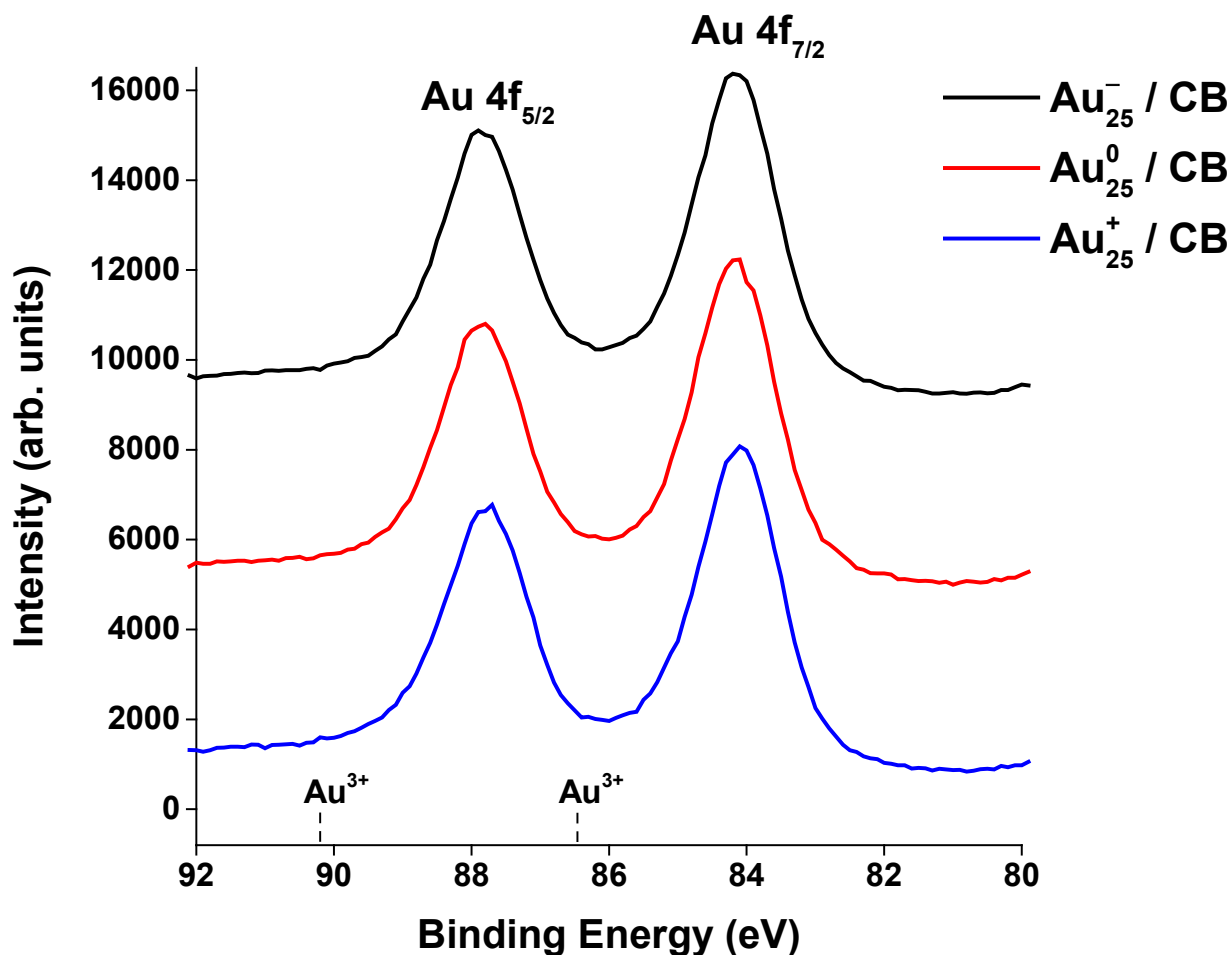


**Figure S2.** Au 4f region X-ray photoelectron spectroscopy (XPS) of the CB-supported Au<sub>25</sub><sup>q</sup> clusters. The spectra are offset for clarity and the expected position of Au<sup>3+</sup>-containing oxide peaks are indicated.

These X-ray photoelectron spectra confirm the absence of Au-oxide species on the Au<sub>25</sub><sup>0</sup> and Au<sub>25</sub><sup>+</sup> surface. We did not detect significant shifts in Au 4f binding energy between the different Au<sub>25</sub><sup>q</sup> charge states. The observed change in electron density between Au<sub>25</sub><sup>q</sup> charge states would apparently be averaged across all 25 Au atoms in the cluster. This difference would be an apparent  $\Delta e^- = -1/25 e^-$  per Au atom for Au<sub>25</sub><sup>0</sup> and  $\Delta e^- = -2/25 e^-$  per Au atom for Au<sub>25</sub><sup>+</sup>. Any spectral shifts associated with these small, apparent  $\Delta e^-$  changes are likely below the resolution of our XPS instrument.

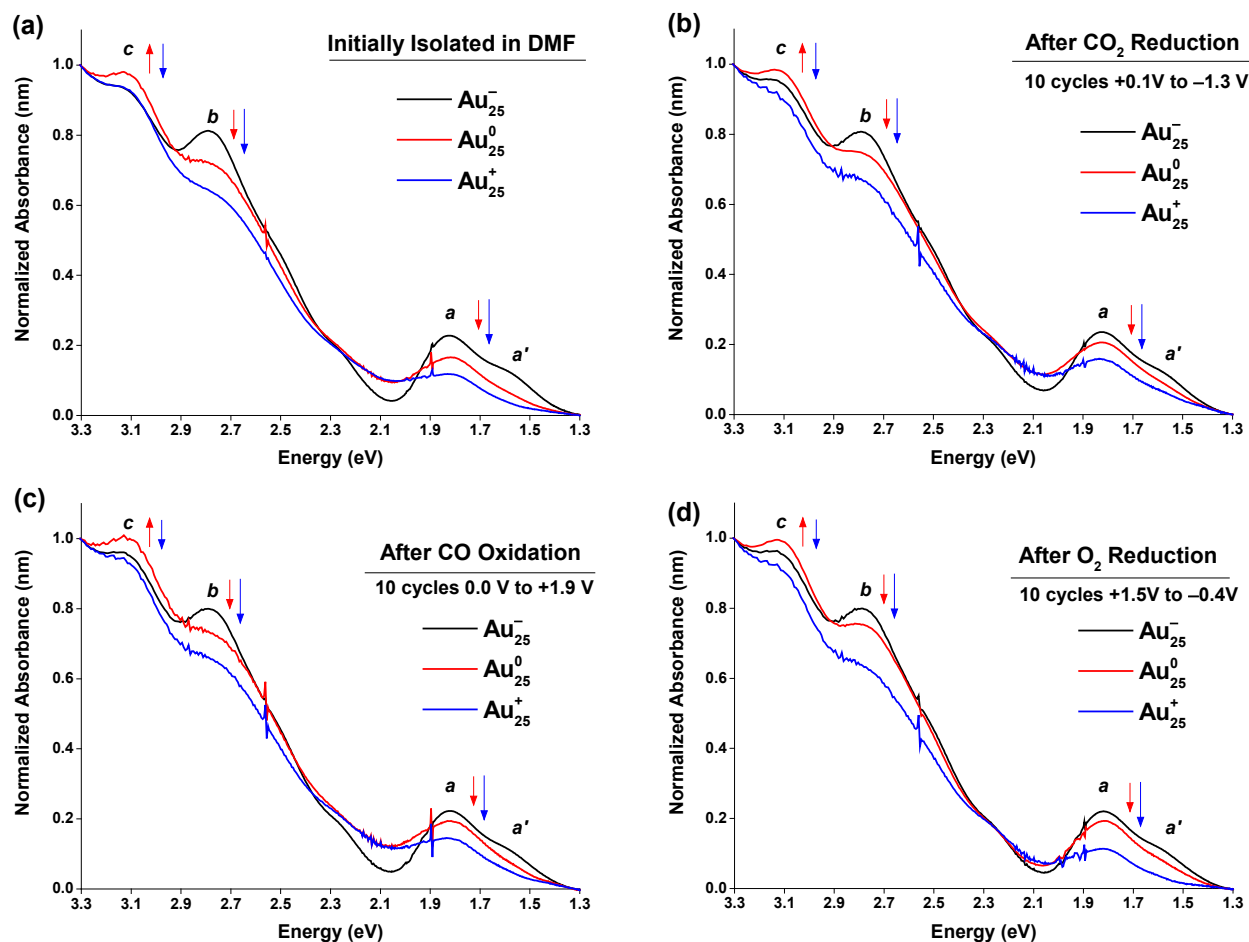


**Figure S3.** Optical absorbance spectra of  $\text{Au}_{25}^q$  charge states (a) initially isolated in DMF, and after electrocatalytic (b)  $\text{CO}_2$  reduction, (c) CO oxidation, and (d)  $\text{O}_2$  reduction. After the electrocatalytic reactions the electrode was rinsed with water, dried under  $\text{N}_2$  and the clusters were extracted back into DMF. The red and blue arrows show the general peak trends between the different  $\text{Au}_{25}^q$  charge states. Retention of characteristic charge state-dependent optical spectra strongly suggest the  $\text{Au}_{25}^q$  clusters were stable during electrocatalytic reactions in aqueous electrolyte.

We characterized the optical absorbance spectra of  $\text{Au}_{25}^q$  clusters before electrocatalytic  $\text{CO}_2$  reduction, CO oxidation and  $\text{O}_2$  reduction reactions. Changes to the characteristic optical spectra would indicate if the cluster changed oxidation states or became degraded during the reaction. Specifically, changes in charge state or cluster degradation would have produced new optical signatures.

$\text{Au}_{25}^q$  charge states were isolated in fast-drying  $\text{CH}_2\text{Cl}_2$  or acetone and dropcast directly onto a glassy carbon electrode. We did not use DMF to isolate the clusters because it dries extremely slowly on the electrode surface. During the dropcasting procedure we shrouded the electrode in flowing  $\text{N}_2$  and protected it from direct light to prevent cluster photo-oxidation. The

dropcast clusters were then cycled between the indicated potentials 10 times at 50 mV/sec in CO<sub>2</sub>, CO or O<sub>2</sub> saturated solution. After the electrocatalytic experiments were complete the electrode was rinsed with DI water and dried under N<sub>2</sub>. The clusters were then extracted off the electrode into DMF and their absorbance spectrum was recorded. These results show the clusters were stable during the electrocatalytic reactions, and we confidently attribute the catalytic activity differences to the particular Au<sub>25</sub><sup>q</sup> cluster's ground state charge.

We would like to point out that charge state stability is unique to aqueous environments, and aqueous electrochemistry cannot resolve discrete Au<sub>25</sub><sup>q</sup> orbitals.<sup>12</sup> Rather, aqueous electrochemical potentials promote the adsorption and reaction of ions and molecules at the cluster surface. Conversely, *nonaqueous* electrochemistry can resolve discrete Au<sub>25</sub><sup>q</sup> orbitals and directly control the cluster charge state.<sup>2, 12-13</sup>

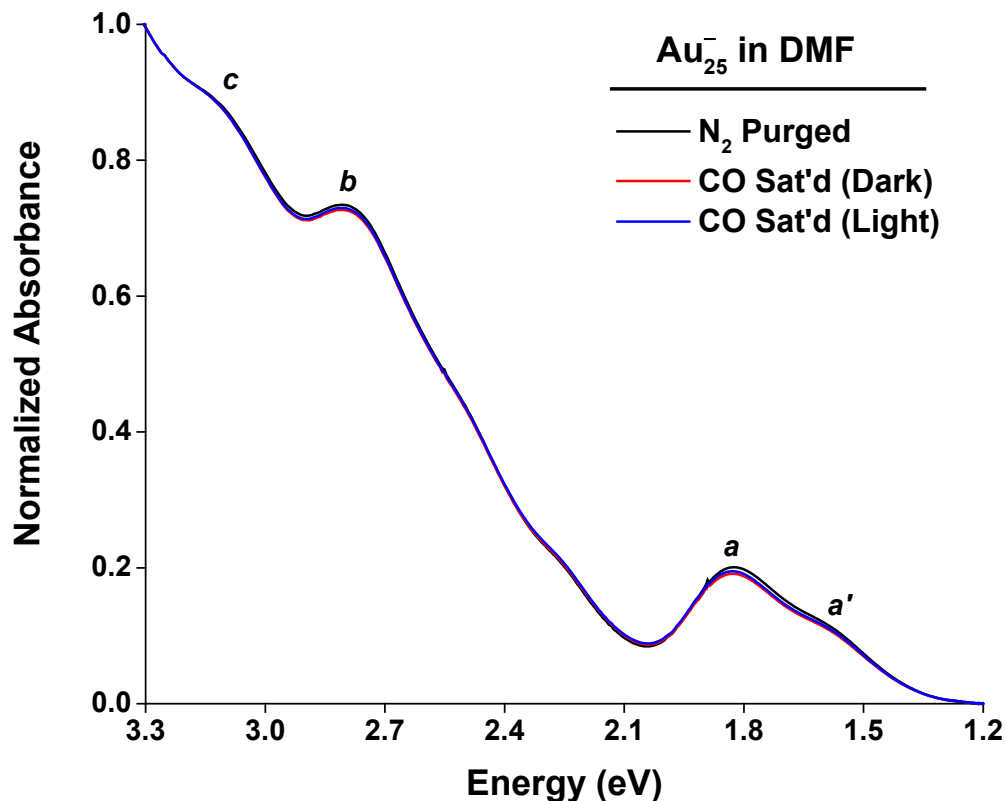


**Figure S4.** Optical absorbance spectrum of Au<sub>25</sub><sup>-</sup> in N<sub>2</sub> purged DMF (black curve), after saturating the solution with CO gas in the dark (red curve), and after saturating the solution with CO during illumination with light containing energy greater than the Au<sub>25</sub><sup>-</sup> HOMO-LUMO energy gap (  $h\nu < 1.9$  eV;  $\lambda > 650$  nm light).

Exposing a Au<sub>25</sub><sup>-</sup> solution to pure CO gas did not induce spectral changes in the absence or presence of light containing energy greater than the cluster HOMO-LUMO gap. This indicates CO gas does not engage in spontaneous charge transfer with the ground-state or excited-state cluster. These results are in line with previous calculations that predict Au<sub>25</sub><sup>q</sup>-CO charge transfer requires removal of cluster ligands.<sup>14</sup> Please see references 2 and 11 for the optical absorbance spectra of Au<sub>25</sub><sup>-</sup> in O<sub>2</sub> and CO<sub>2</sub> saturated DMF.

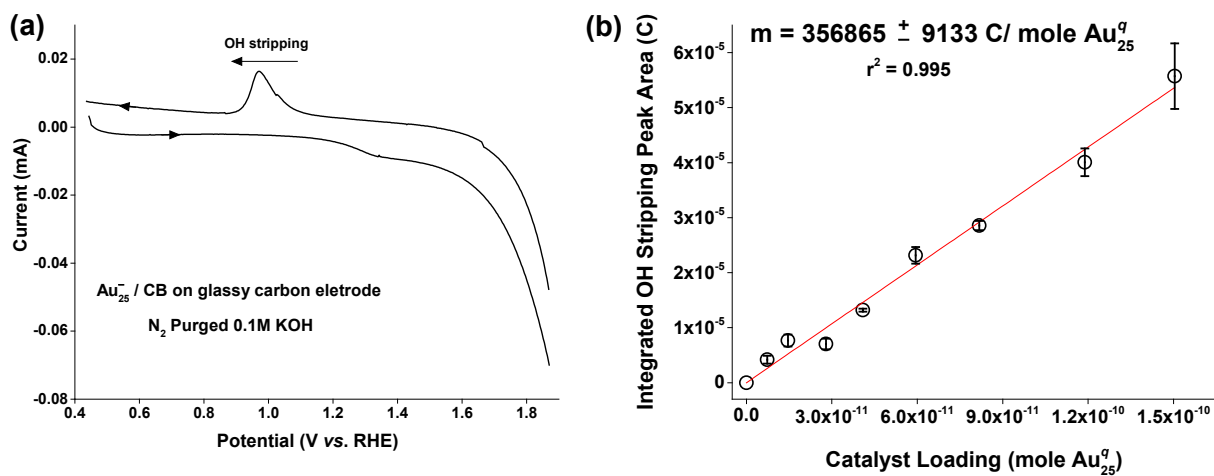


**Figure S5.** (a) RDE voltammogram of Au<sub>25</sub><sup>-</sup>/CB in N<sub>2</sub> purged KOH showing the OH<sup>-</sup> stripping peak at approximately +1.0 V vs. RHE ( $\omega = 2500$  rpm; 50 mV/s scan rate). (b) Integrated OH stripping peak area vs. catalyst loading. Error bars at each catalyst loading represent three OH stripping experiments with freshly deposited Au<sub>25</sub><sup>q</sup>/CB.

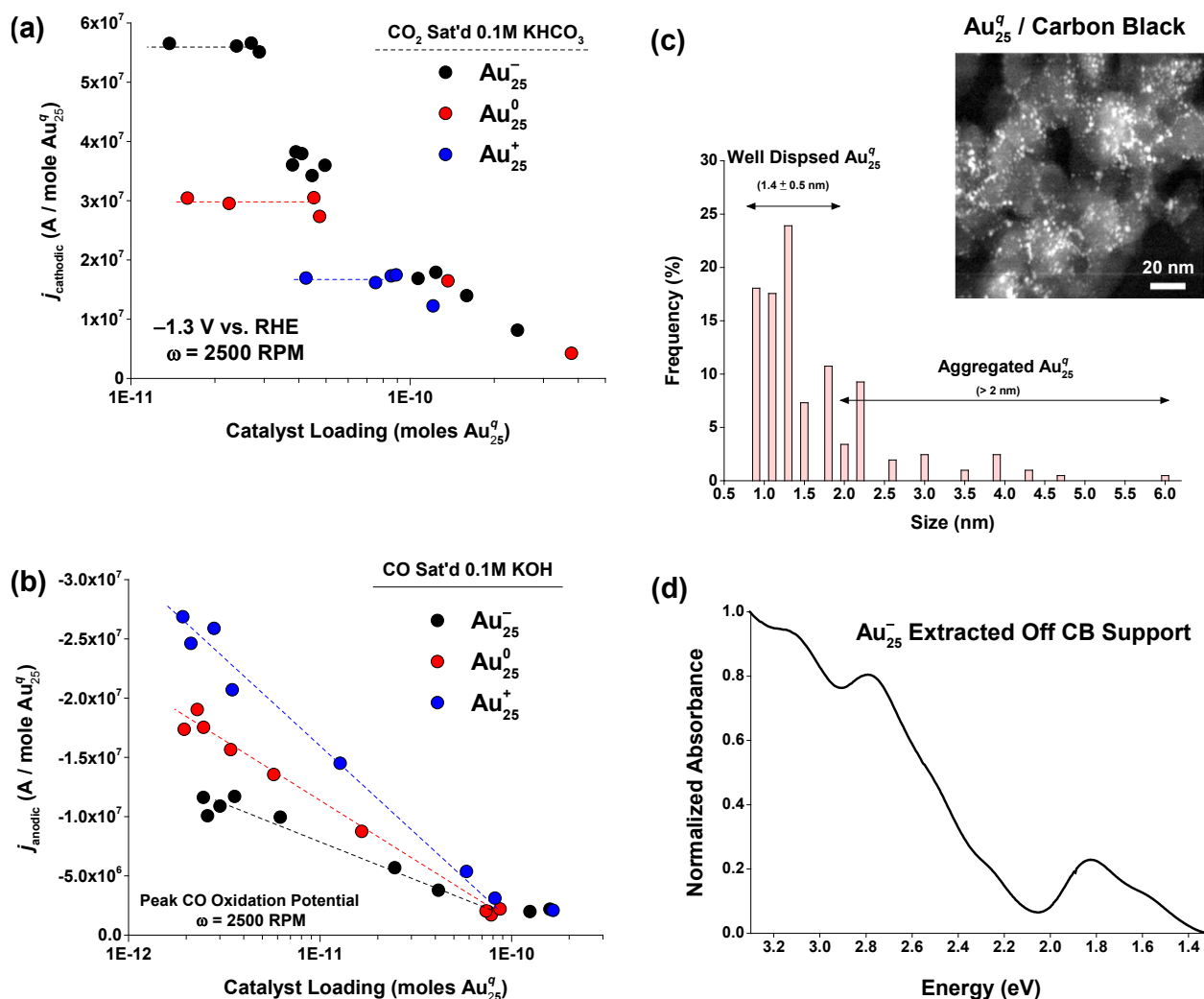


**Figure S6.** Variation in measured current density  $j$  (A / mole Au<sub>25</sub><sup>q</sup>) vs. catalyst loading (moles Au<sub>25</sub><sup>q</sup>) for (a) CO<sub>2</sub> reduction (measured at -1.3 V vs. RHE) and (b) CO oxidation reactions (measured at peak CO oxidation potential). Data points represent the raw data collected from polarization curves and the dashed lines serve as a guide to the eye. (c) TEM image and particle size distribution of an Au<sub>25</sub><sup>q</sup>/CB sample in the high Au<sub>25</sub><sup>q</sup> loading regime. (d) Optical absorbance spectra of Au<sub>25</sub><sup>-</sup> extracted back off the CB support. Retention of optical absorbance spectra indicates the larger Au<sub>25</sub><sup>q</sup> aggregates in figure S6c are likely closely spaced, individual Au<sub>25</sub><sup>q</sup> clusters, and necessarily rules out the clusters sintering into larger particles.

We noticed an inverse relationship between catalyst loading and catalytic current density for CO<sub>2</sub> reduction and CO oxidation reactions. The current density  $j$  (A / mol Au<sub>25</sub><sup>q</sup>) increased as the catalyst loading (mol Au<sub>25</sub><sup>q</sup>) decreased. Catalyst loadings were adjusted by varying the ratio of Au<sub>25</sub><sup>q</sup> to CB support. Loadings were quantified by integrating the OH<sup>-</sup> stripping peak (see figure S5 on the previous page). The trend of increasing current density eventually stabilized for

CO<sub>2</sub> reduction. Catalyst loadings from the stabilized loading regime were chosen to compare the CO<sub>2</sub> activity of differently charged Au<sub>25</sub><sup>q</sup> clusters.

No current density stabilization was observed for the CO oxidation reaction within the range of accurate OH stripping peak area measurement. Equivalent Au<sub>25</sub><sup>q</sup> loadings between 2x10<sup>-12</sup> and 4x10<sup>-12</sup> moles were used for comparison of CO oxidation activity.

The data in figure S6a,b support predictions that closely spaced or aggregated nanocatalysts will have overlapping diffusion regions.<sup>15</sup> Such “catalyst crowding” limits the transport of reactants to the catalyst surface and effectively lowers the apparent catalytic activity of the material. Decreasing the catalyst loading increases the spacing between individual particles and lessens the diffusional overlap. Therefore, lowering the catalyst loading will increase reactant access to each Au<sub>25</sub><sup>q</sup> cluster and increase the observed catalytic current density. The trends in figure S6a,b highlight that care that must be taken when comparing the electrocatalytic activity of supported catalysts, as high catalyst loading can cause “catalyst crowding” and artificially lower the apparent activity.

Figure S6c presents a dark-field transmission electron microscope (TEM) image and a particle size histogram of the CB-supported Au<sub>25</sub><sup>q</sup> clusters. A high Au<sub>25</sub><sup>q</sup> loading was used to facilitate TEM imaging. The Au<sub>25</sub><sup>q</sup> clusters appear as small bright spots and the CB support appears dark. In this high loading regime we found a combination of well-dispersed, apparently isolated Au<sub>25</sub><sup>q</sup> clusters (1.4±0.5 nm; n=189) and larger Au<sub>25</sub><sup>q</sup> aggregates. This cluster size is consistent with the ~1nm diameter expected from the Au<sub>25</sub><sup>q</sup> crystal structure<sup>1, 16</sup> and other TEM images of supported Au<sub>25</sub> clusters.<sup>17</sup>

Pradeep and coworkers noted that Au<sub>25</sub><sup>q</sup> clusters can experience electron-induced sintering during TEM imaging.<sup>18</sup> To avoid cluster damage we used the lowest possible electron dosage that provided adequate contrast for imaging, and we did not observe particle sintering during TEM imaging. Au<sub>25</sub><sup>q</sup> clusters retained their characteristic optical spectra once extracted off the CB support (Figure S6d), whereas sintered Au<sub>25</sub><sup>q</sup> clusters should lose their characteristic, molecule-like optical spectra and develop plasmon resonances associated with larger Au nanoparticles. The retention of the Au<sub>25</sub><sup>q</sup> optical spectrum indicates the Au<sub>25</sub><sup>q</sup> aggregates seen in figure S6c contain multiple, closely spaced ~1nm clusters. This apparent Au<sub>25</sub><sup>q</sup> aggregation in a high loading sample correlates well with the “catalyst crowding” concept presented in figures S6a,b.

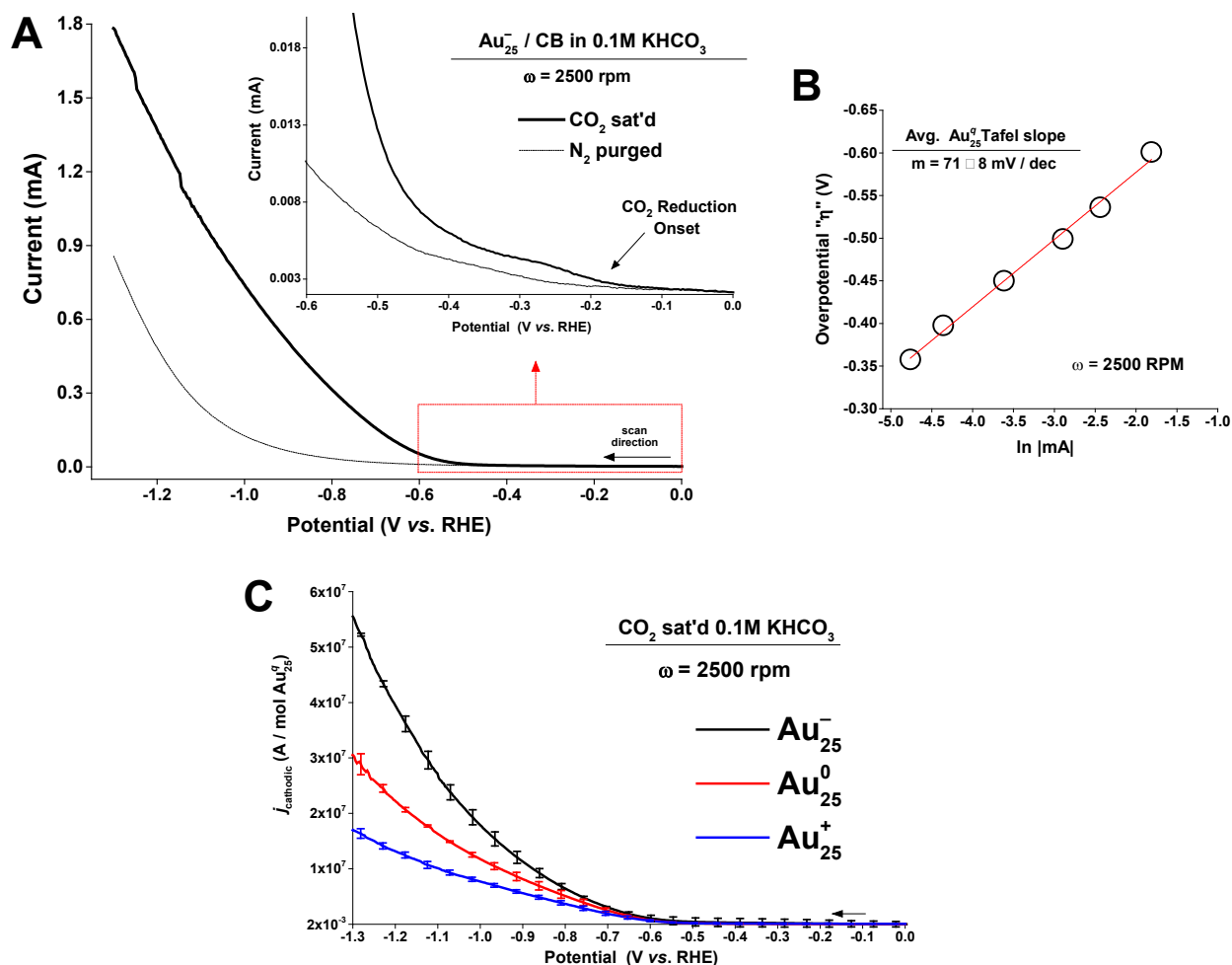
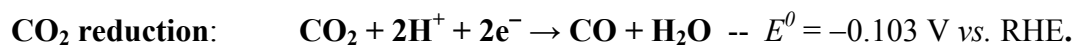


**Figure S7.** (a) Polarization curves of CB-supported  $\text{Au}_{25}^-$  in  $\text{N}_2$  purged (dashed line) and  $\text{CO}_2$  saturated (solid curve)  $0.1\text{M KHCO}_3$ . The inset shows the onset of  $\text{CO}_2$  reduction at  $-0.223 \pm 0.049 \text{ V vs. RHE}$ . A relatively high catalyst loading of  $5 \times 10^{-11}$  moles  $\text{Au}_{25}^-$  was used in panel A to demonstrate the  $\text{CO}_2$  reduction onset. (b) Representative Tafel plot of CB-supported  $\text{Au}_{25}^-$  in  $\text{CO}_2$  saturated  $0.1\text{M KHCO}_3$ . (c) Average polarization curves of  $\text{Au}_{25}^q$  in  $\text{CO}_2$  saturated  $0.1\text{M KHCO}_3$  ( $\omega = 2500 \text{ rpm}$ ). Cluster loadings for panels c and were within the stable catalyst loading vs. current density regime for each  $\text{Au}_{25}^q$  cluster to ensure accurate comparison; see figures S5 and S6 for further details concerning catalyst loading vs. catalytic current density. Error bars are from three separate experiments with freshly deposited  $\text{Au}_{25}^q/\text{CB}$ .

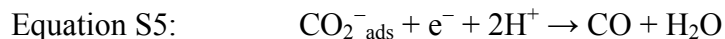
Figure S7a shows the onset for  $\text{CO}_2$  reduction. Equivalent onset potentials of  $E_{\text{onset}} = -0.223 \pm 0.049 \text{ V vs. RHE}$  were determined for the differently charged  $\text{Au}_{25}^q$  clusters. Adsorbed  $\text{CO}_2$  is reversibly reduced into  $\text{CO}_2^-$  between  $E = -0.2 \text{ V}$  and  $-0.4 \text{ V}$  (Equation S1).  $\text{H}^+$  coadsorption /  $\text{H}_{\text{ads}}$  formation begins at approximately  $E = -0.5 \text{ V vs. RHE}$  (Equation S2) as evidenced by the onset of minor  $\text{H}_2$  evolution.<sup>11</sup> Dramatically increased  $\text{CO}$  production rates coincide with  $\text{H}^+$  coadsorption /  $\text{H}_{\text{ads}}$  formation and  $\text{CO}_2$  reduction proceeds through Equations

S3 and S4. This mechanism was determined from the potential product distribution described in reference 11.

Figure S7b shows a representative Tafel plot for CO<sub>2</sub> reduction at Au<sub>25</sub><sup>-</sup>. Equivalent Tafel slopes indicate a common mechanism for CO<sub>2</sub> reduction at the Au<sub>25</sub><sup>q</sup> clusters. Tafel slopes of 71 ± 8 mV dec<sup>-1</sup> are close to the reversible limit of 59 mV dec<sup>-1</sup>. Such Tafel slope values indicate a mechanism involving an initial reversible electron transfer to CO<sub>2</sub> (Equation S1) followed by a rate-determining chemical step.<sup>19</sup>



**Alternative CO<sub>2</sub> Reduction mechanism (no H<sub>ads</sub>; low potential regime, very slow)**



We note that an alternative, low-overpotential CO<sub>2</sub> reduction mechanism can occur in the absence of H<sub>ads</sub> (Equation S5). In the low overpotential regime (before H<sub>ads</sub> formation) the initial electron transfer to CO<sub>2</sub> is reversible (Equation S1). However, CO<sub>2</sub><sup>-</sup><sub>ads</sub> can be reduced into CO through sequential proton capture and electron transfer steps. This low-potential process is kinetically sluggish as seen from potential-dependent product analysis<sup>11</sup> and small CO<sub>2</sub> reduction current (figure S7a).

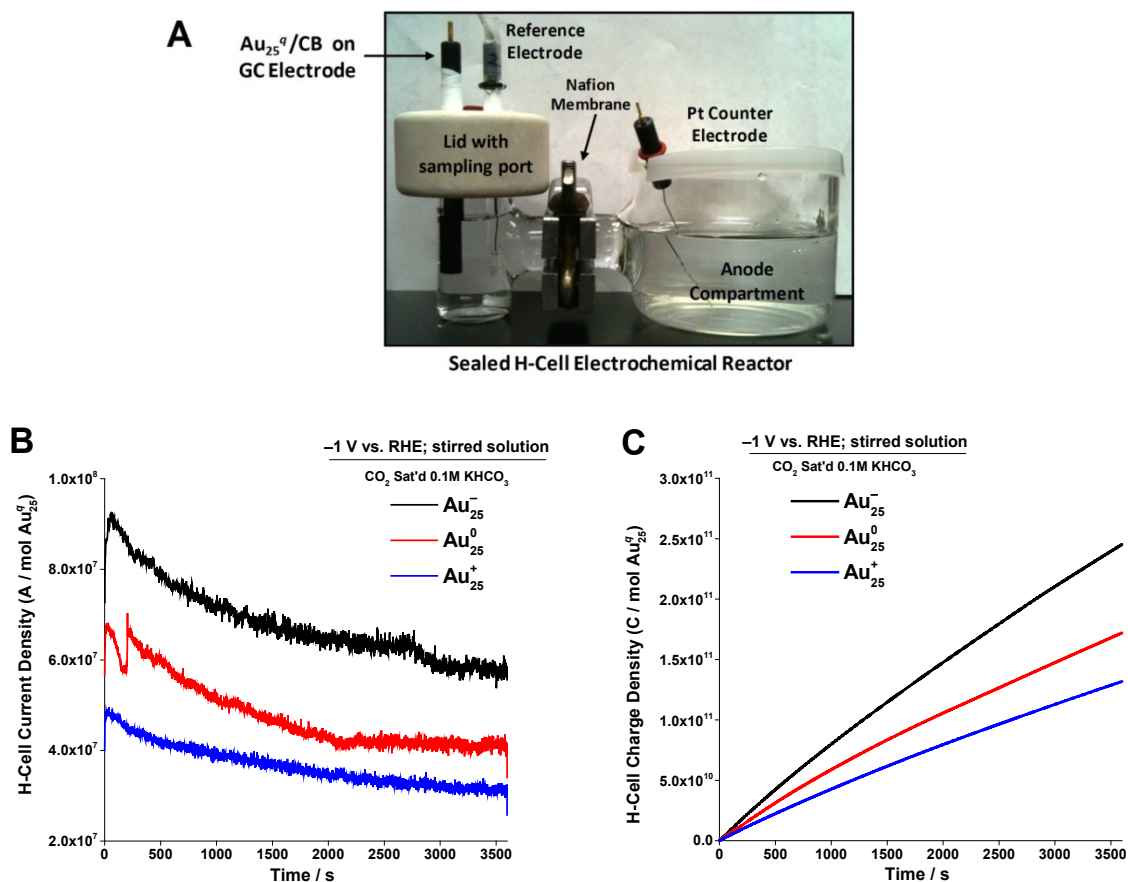


**Figure S8.** (a) Photograph of the H-Cell electrochemical reactor for analysis of CO<sub>2</sub> reduction products. Representative (b) current density (A / mole Au<sub>25</sub><sup>q</sup>) and (c) charge density (C / mole Au<sub>25</sub><sup>q</sup>) vs. time plots of the Au<sub>25</sub><sup>q</sup> clusters at -1 V in stirred, CO<sub>2</sub> saturated 0.1M KHCO<sub>3</sub>. Catalyst loadings between 2x10<sup>-12</sup> and 4x10<sup>-12</sup> mole Au<sub>25</sub><sup>q</sup> were used for H-Cell experiments.

An electrochemical H-cell reactor was used to quantify reaction products. The cell consisted of two chambers separated by a Nafion cation exchange membrane. One chamber was gas-tight and contained a stationary GC electrode and an Ag/AgCl reference electrode. The other compartment contained a Pt-wire counter electrode. This configuration keeps the reaction products in the working-electrode chamber, but the Nafion membrane still allows current flow *via* proton conduction. The solution was vigorously stirred at a constant rate and -1V vs. RHE was applied to the working electrode for 1 hour; this potential was previously identified as the optimal H-cell potential for selective CO<sub>2</sub> → CO conversion.<sup>11</sup> Products in the headspace and electrolyte were analyzed with gas chromatography after one hour of electrolysis (values shown below).

The H-Cell reactor produced current densities and TOFs that were approximately 3-4 times higher than RDE polarization experiments. These higher current densities resulted from the experimental setup. For example, the H-Cell used a stationary GC working electrode placed ~5

mm above a stir bar to prevent bubble build-up during electrolysis. The rapidly stirred solution produced the higher current density and TOFs compared with the RDE experiments. The retention of charge state-dependent CO<sub>2</sub> activity indicates the Au<sub>25</sub><sup>q</sup> clusters were stable during CO<sub>2</sub> reduction.

<b>CO Production Rates from H-Cell Reactor</b>						
	<b>mol Au<sub>25</sub><sup>q</sup></b>	<b>CO TOF (molec./Au<sub>25</sub><sup>q</sup>/s)</b>	<b>CO selectivity (%)</b>	<b>CO FE (%)</b>	<b>ECSA (cm<sup>-2</sup><sub>Au</sub>)</b>	<b>CO Production Rate (mmol/cm<sub>Au</sub><sup>2</sup>/hr)</b>
<b>Au<sub>25</sub><sup>-</sup></b>	(1.93±0.06)×10 <sup>-12</sup>	328 ± 10	97.7 ± 0.8	99 ± 4	0.00177±0.00005	1.29 ± 0.04
<b>Au<sub>25</sub><sup>0</sup></b>	(2.8±0.2)×10 <sup>-12</sup>	213 ± 5	96 ± 1	82 ± 7	0.0026±0.0002	0.84 ± 0.2
<b>Au<sub>25</sub><sup>+</sup></b>	(3.6±0.2)×10 <sup>-12</sup>	156 ± 9	97.9 ± 0.5	81 ± 1	0.0033±0.0002	0.62 ± 0.04

Au<sub>25</sub><sup>-</sup> converted CO<sub>2</sub> into CO with 99 ± 4% Faradaic efficiency (FE) at -1V. Minor amounts of H<sub>2</sub> were also evolved. Lower FEs were observed for Au<sub>25</sub><sup>0</sup> (82 ± 7% FE) and Au<sub>25</sub><sup>+</sup> (81 ± 1% FE), although their CO selectivities were still high. Control experiments showed the CB support contributed less than 2% of the observed CO, and electrolysis in N<sub>2</sub> purged solutions produced H<sub>2</sub> and trace amounts of CO (< 0.1% of that formed during electrolysis in CO<sub>2</sub> saturated solutions). Faradaic Efficiencies (FE) were calculated from the detected reaction products, the integrated reaction charge, Faraday's constant (96485 C/mol e<sup>-</sup>) and the number of electrons required for product formation (CO = 2e<sup>-</sup>). For example:

$$FE = 100\% * \left\{ \frac{\text{detected mol CO}}{[\text{electrolysis charge (C)}] \left( \frac{1 \text{ mol } e^-}{96485 \text{ C}} \right) \left( \frac{\text{CO molecule}}{2e^-} \right)} \right\}$$

We previously normalized our reaction rates to the electrochemical surface area of the Au<sub>25</sub><sup>q</sup> cluster using the value for bulk Au (390 μC/cm<sup>2</sup><sub>Au</sub>).<sup>5</sup> The ECSA and ECSA-normalized values are summarized in the table above. The ECSA-normalized CO production rate for Au<sub>25</sub><sup>-</sup> is statistically identical to our previously determined value of 1.26 mmol/cm<sup>2</sup><sub>Au</sub>/hr.<sup>11</sup> However, it is difficult to estimate the TOF from these values because one must assume bulk areal density of gold. Our current method of precisely measuring the moles of Au<sub>25</sub><sup>q</sup> on the electrode surface (figure S5) provides more accurate TOF estimates.

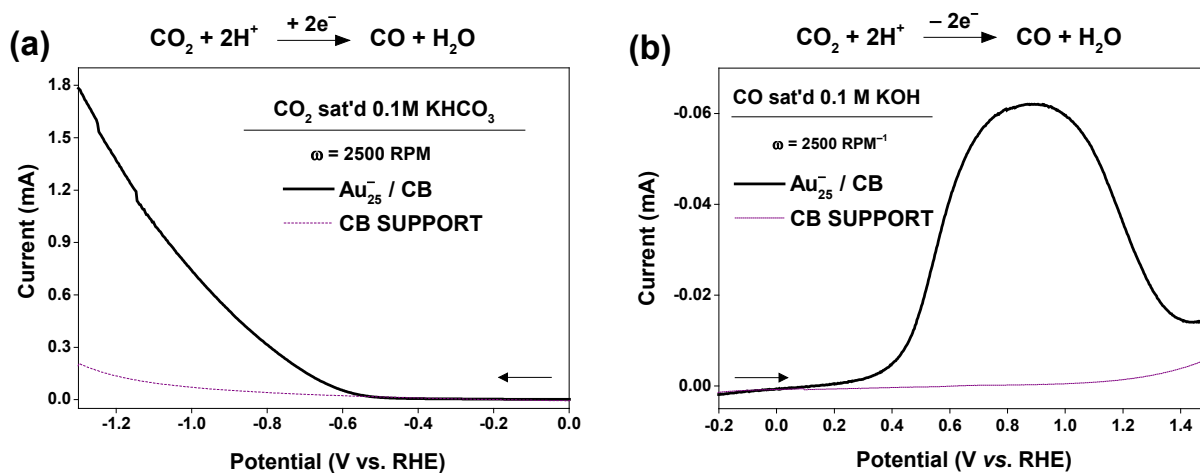
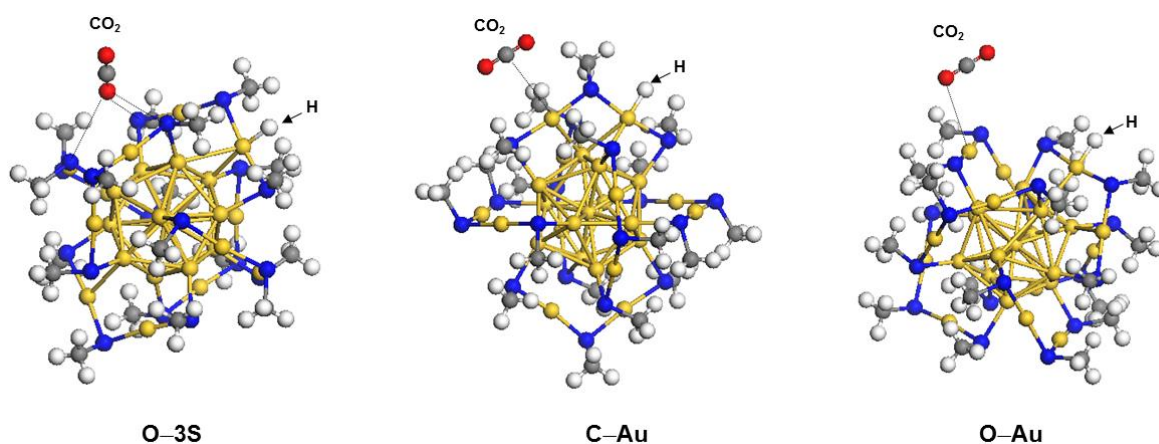


**Figure S9.** Comparison of (a) CO<sub>2</sub> reduction and (b) CO oxidation at CB-supported Au<sub>25</sub><sup>-</sup> and the catalyst-free CB support. The CB support shows negligible activity for CO<sub>2</sub> reduction and CO oxidation compared with Au<sub>25</sub><sup>g</sup>.



CO <sub>2</sub> + H <sup>+</sup> Coadsorption Energies (eV)				
	<u>O-3S</u>	<u>C-Au</u>	<u>O-Au</u>	<u>Average</u>
<b>Au<sub>25</sub><sup>-</sup></b>	-12.23	-12.24	-12.27	-12.25 ± 0.02
<b>Au<sub>25</sub><sup>0</sup></b>	-9.96	-10.05	-10.09	-10.03 ± 0.07
<b>Au<sub>25</sub><sup>+</sup></b>	-8.32	-7.91	-8.06	-8.06 ± 0.23

**Figure S10.** Ball-and-stick representations of CO<sub>2</sub> + H<sup>+</sup> coadsorption geometries and their binding energies. The O-3S coadsorption geometry is presented as a space-filled model in main text Figure 2c. Atom colors: Au: gold, S: blue, C: grey, H: white, O: red.

We compared CO<sub>2</sub> + H<sup>+</sup> coadsorption on realistic, fully ligand-protected Au<sub>25</sub>(SCH<sub>3</sub>)<sub>18</sub><sup>q</sup> cluster models ( $q = -1, 0, +1$ ). Our calculations identified several common coadsorbed states at the differently charged Au<sub>25</sub><sup>q</sup> clusters. One such state includes H bound to one ligand-shell Au atom of the negatively charged Au<sub>25</sub><sup>-</sup> cluster with calculated H-Au distance of 1.61 Å. CO<sub>2</sub> coordinates with three ligand-shell S atoms in the previously identified adsorption pocket<sup>11</sup> with O-S distances ranging between 3.55-3.71 Å. This coadsorption geometry is labeled as O-3S in figure S10. Two additional stable configurations were identified and H and CO<sub>2</sub> were both bound to ligand-shell Au atoms. CO<sub>2</sub> attached to the ligand-shell Au atom with its C atom (C-Au configuration) or O atom (O-Au configuration). In both cases the O-C-O bond axis of the molecule is roughly parallel with the S-Au-S moiety in the ligand. The structure of the cluster remained intact in all CO<sub>2</sub> + H<sup>+</sup> coadsorption geometries.

The binding energies are summarized in figure S10, and the stability of different coadsorbed states were equivalent at any one Au<sub>25</sub><sup>q</sup> charge state. An important finding here is that binding energies of coadsorbed states at Au<sub>25</sub><sup>-</sup> are consistently larger. This finding represents more stable reactant adsorption at the negatively charged cluster. The relationship between TOF and CO<sub>2</sub> + H<sup>+</sup> binding energy (Figure 2b in the main text) highlight that reactant adsorption is a key parameter affecting the CO<sub>2</sub> reduction rate.

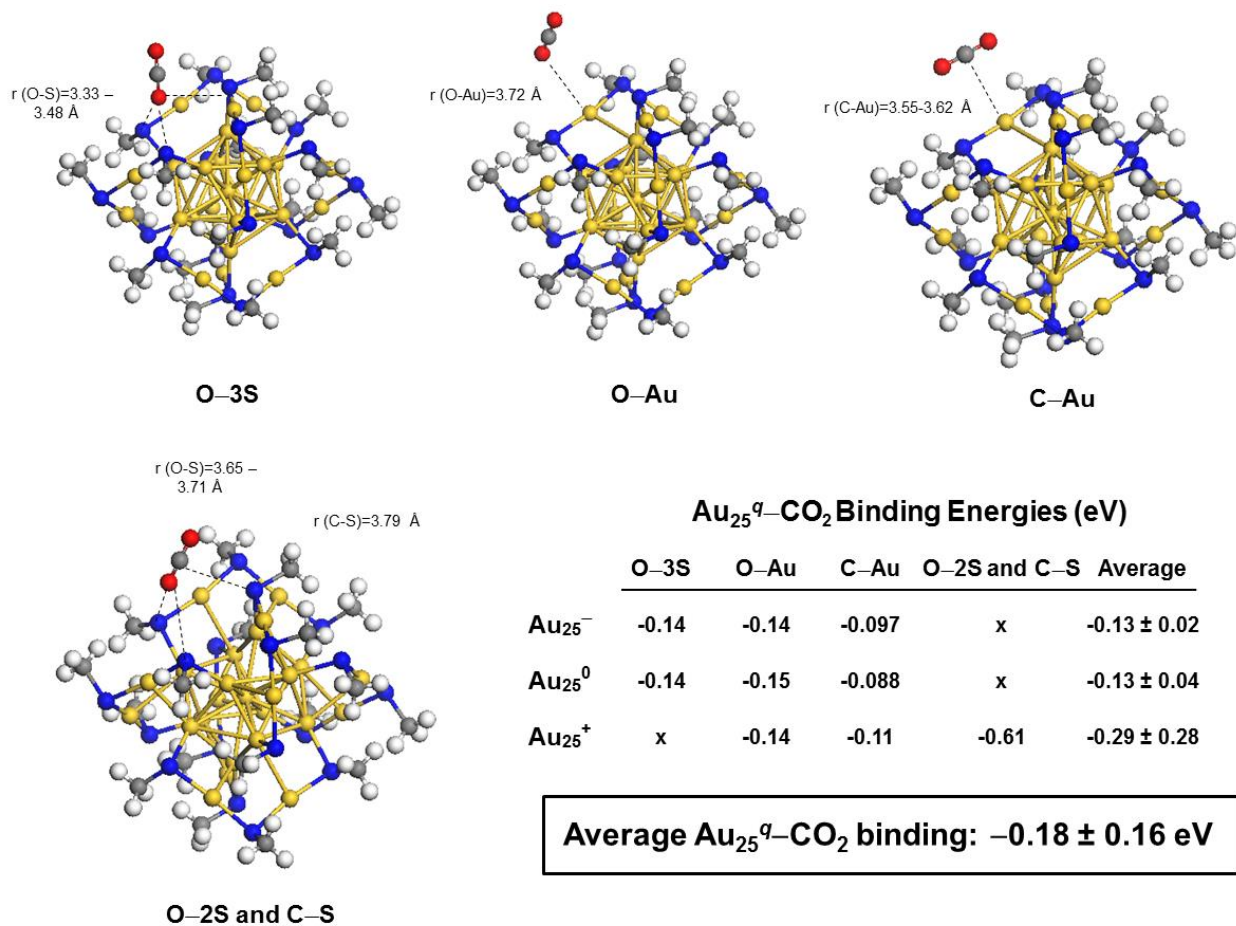
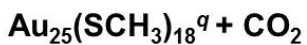


**Figure S11.** Ball-and-stick representations and binding energies of the singly-bound  $\text{Au}_{25}^q\text{-CO}_2$  system. Atom colors: Au: gold, S: blue, C: grey, H: white, O: red.

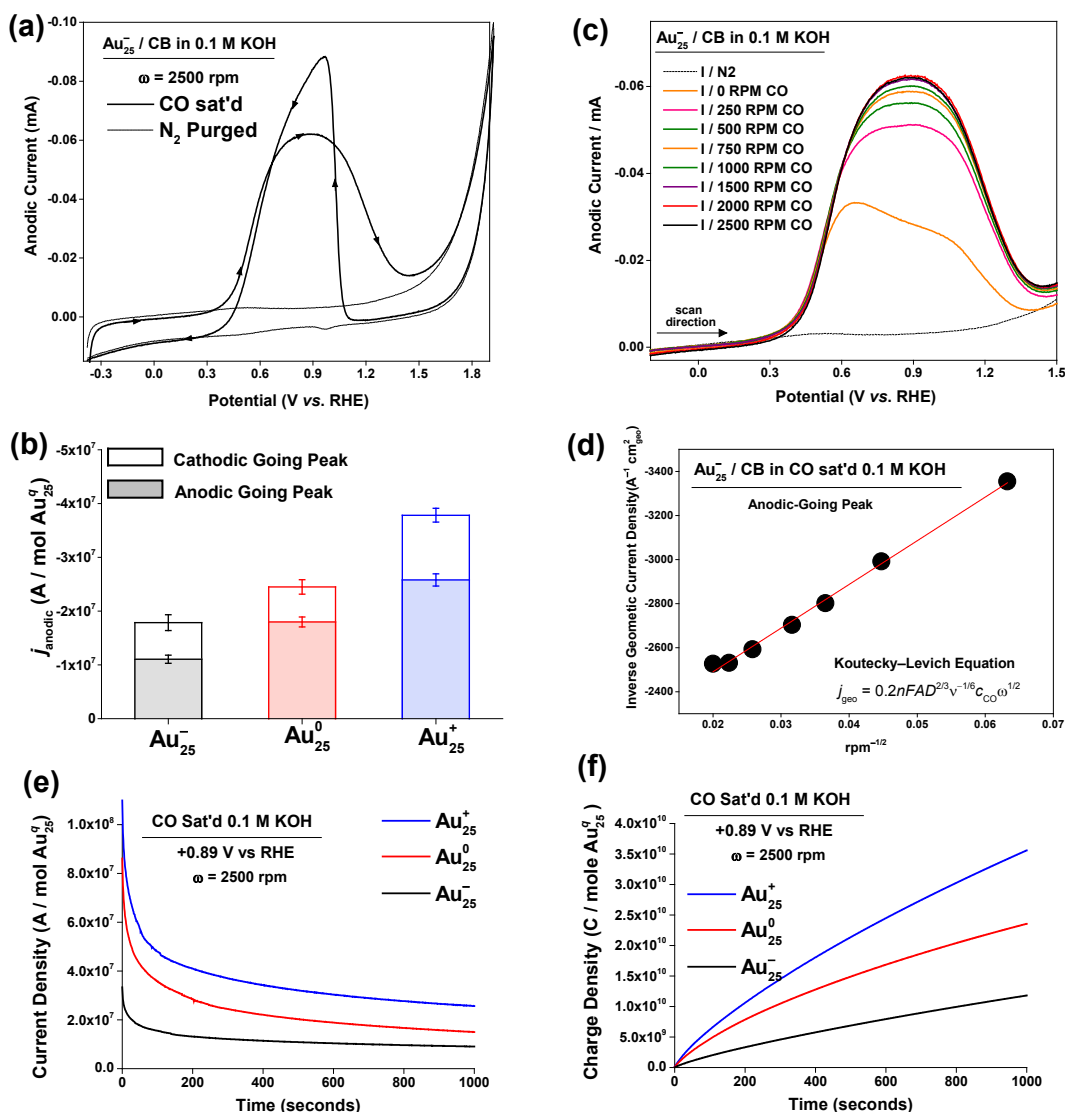
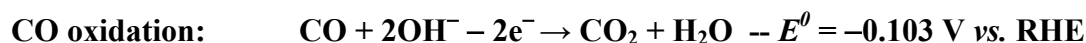


**Figure S12.** (a) Cyclic voltammograms of CB-supported  $\text{Au}_{25}^-$  in CO saturated and  $\text{N}_2$  purged 0.1M KOH ( $\omega = 2500$  rpm;  $v = 50$  mV/s). (b) Comparison of CO oxidation current density from the anodic- and cathodic-going scan directions; error bars are from three separate measurements with freshly deposited  $\text{Au}_{25}^q/\text{CB}$ . (c) Representative RDE curves at different rotation rates. (d) Levich analysis of RDE polarization curves.<sup>20</sup> (e,f) Constant potential electrolysis of CO at +0.89 V vs. RHE, electrode rotation rate  $\omega = 2500$  rpm. Equivalent catalyst loadings of  $2\text{-}4 \times 10^{-12}$  mole  $\text{Au}_{25}^q$  were used for CO activity comparison and TOF determinations (see figs. S5 and S6).



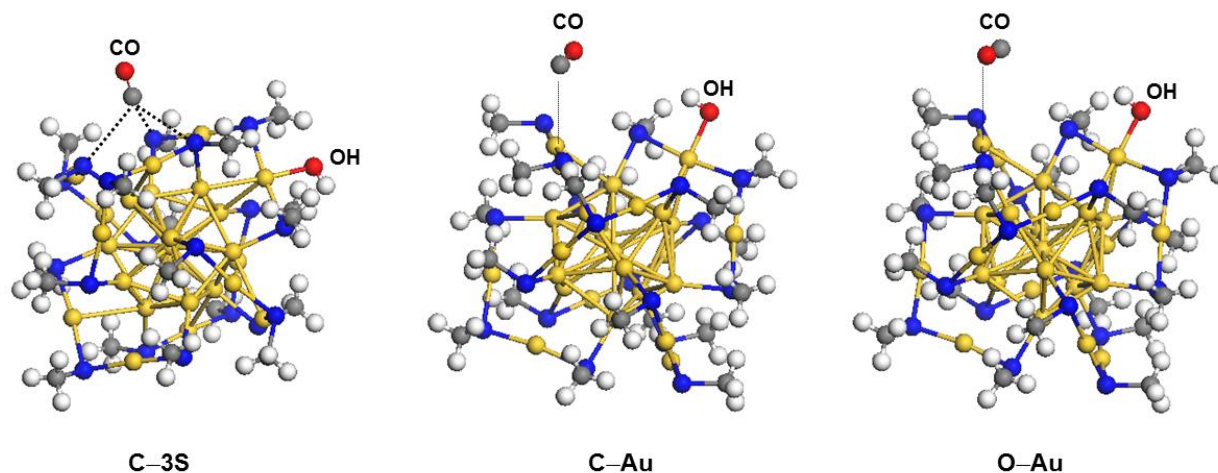
It is generally agreed that CO oxidation proceeds through a Langmuir-Hinshelwood mechanism with adsorbed OH<sup>-</sup> acting as the oxidant (Equations S6-S8).<sup>3, 21</sup> This means the CO oxidation rate depends on the availability of adsorbed OH. In fact, the large overpotentials required for CO oxidation stem from OH adsorption at the catalyst surface.<sup>22</sup> The cyclic voltammograms in Figure S12a show CB-supported Au<sub>25</sub><sup>-</sup> in N<sub>2</sub> purged and CO saturated 0.1 M KOH ( $\omega = 2500$  rpm;  $v = 50$  mV/s). Equivalent anodic-going Tafel slopes of  $95 \pm 17$  mV/dec were found for the differently charged Au<sub>25</sub><sup>q</sup> clusters, which are consistent with other Au catalysts.<sup>19, 21</sup>

The CO oxidation current decreased beyond +1V. This phenomenon has previously been attributed to preferential OH<sup>-</sup> adsorption blocking CO sites.<sup>22</sup> This interpretation is reasonable because the electrochemical OH<sup>-</sup> stripping peak occurs at approximately +1V with CB-supported Au<sub>25</sub><sup>q</sup> clusters (figure S5 and Table S1). Water splitting above  $\sim 1.6$  V produced a large current increase. In the reverse, cathodic (negative)-going potential sweep a peak represents the oxidation of CO by preadsorbed OH. Figure S12b shows reproducible CO oxidation peak current densities in both scan directions.

Figures S12c,d present typical positive-going RDE polarization curves and their analysis with Levich plots.<sup>20</sup> The RDE polarization curves were analyzed using the equation  $j_{geo} = 0.2nFA D^{2/3} v^{-1/6} C \omega^{1/2}$ . Here,  $j_{geo}$  is the limiting geometric current density (normalized to the geometric area of the electrode),  $n$  is the number of electrons transferred in the electrocatalytic reaction,  $F$  is the Faraday constant (96485 C/mol e<sup>-</sup>),  $A$  is the geometric area of the electrode (0.1963 cm<sup>2</sup>),  $D^{2/3}$  is the diffusion coefficient of CO in water ( $2 \times 10^{-5}$  cm<sup>2</sup>/s),  $v$  is the kinetic viscosity of water (0.01 cm<sup>2</sup>/s),  $C$  is the concentration of dissolved CO in the bulk solution ( $1 \times 10^{-6}$  mol/cm<sup>3</sup>), and  $\omega$  is the rotation rate in rpm (250–2500 rpm).<sup>3a</sup> A constant of 0.2 is used when the rotation rate is described in rpm.<sup>23</sup> A plot of the inverse geometric current density vs. the inverse rotation rate produces a slope proportional to the electron transfer number  $n$ .<sup>20</sup> Analysis of anodic (positive)-going RDE polarization curves confirmed the complete oxidation of CO at the differently charged Au<sub>25</sub><sup>q</sup> clusters with equivalent electron transfer numbers of  $n = 2.08 \pm 0.06$  e<sup>-</sup>. This value is consistent with Equations S6-S8.

The CO oxidation peak in the reverse, cathodic-going sweep produced an electron transfer number of  $n = 1.49 \pm 0.11$  e<sup>-</sup>. This smaller value represents the oxidation of CO by OH groups that were already adsorbed during the forward-going sweep. The oxidation peak in the reverse, negative-going sweep is very sharp because CO is rapidly oxidized by preadsorbed OH. The cathodic-going peak is a special consequence of preferential OH<sup>-</sup> adsorption at large positive potentials, and it is not typically used for determining electron transfer numbers, Tafel slopes, or reaction rates.<sup>3, 21</sup>

Figures S12e,f show that charge state dependent CO oxidation activity was sustained during constant potential electrolysis. The retention of charge state-dependent CO activity indicates the Au<sub>25</sub><sup>q</sup> charge state influences reactivity over extended periods of time.



CO + OH<sup>-</sup> Coadsorption Energies (eV)

	<u>C-3S</u>	<u>C-Au</u>	<u>O-Au</u>	<u>Average</u>
<b>Au<sub>25</sub><sup>-</sup></b>	-0.01	x	x	-0.01
<b>Au<sub>25</sub><sup>0</sup></b>	-2.44	-2.35	-2.35	-2.38 ± 0.05
<b>Au<sub>25</sub><sup>+</sup></b>	-4.91	-4.66	-4.71	-4.76 ± 0.13

**Figure S13.** Ball-and-stick representations of CO + OH<sup>-</sup> coadsorption geometries at Au<sub>25</sub><sup>q</sup> and their binding energies. The C-3S coadsorption geometry is presented as a space-filled model in main text Figure 2F. Atom colors: Au: gold, S: blue, C: grey, H: white, O: red.

Our DFT calculations predict several CO + OH<sup>-</sup> coadsorbed states. The “C-3S” coadsorbed state was common among all three Au<sub>25</sub><sup>q</sup> charges states. Here, OH<sup>-</sup> adsorbs at a ligand-shell Au atom with a O-Au distance of 2.13 Å. CO coordinates with three S atoms in the ligand shell with C-S distance ranging from 3.56 to 3.78 Å. This was the only coadsorbed state identified for Au<sub>25</sub><sup>-</sup>. Two additional coadsorbed states were identified for Au<sub>25</sub><sup>0</sup> and Au<sub>25</sub><sup>+</sup>. In both cases CO adsorbed to one Au atom in the ligand shell through its C atom (“C-Au” configuration) or O atom (“O-Au” configuration). The binding energies are summarized in figure S13, and the different coadsorbed states have equivalent energies at any one particular Au<sub>25</sub><sup>q</sup>. A direct relationship between CO + OH<sup>-</sup> adsorption strength and reaction TOF was observed (Figure 2e of the main text). This indicates cationic Au<sub>25</sub><sup>+</sup> clusters enhance CO oxidation rates by stabilizing CO + OH<sup>-</sup> coadsorption.

### $\text{Au}_{25}(\text{SCH}_3)_{18}^q + \text{CO}$

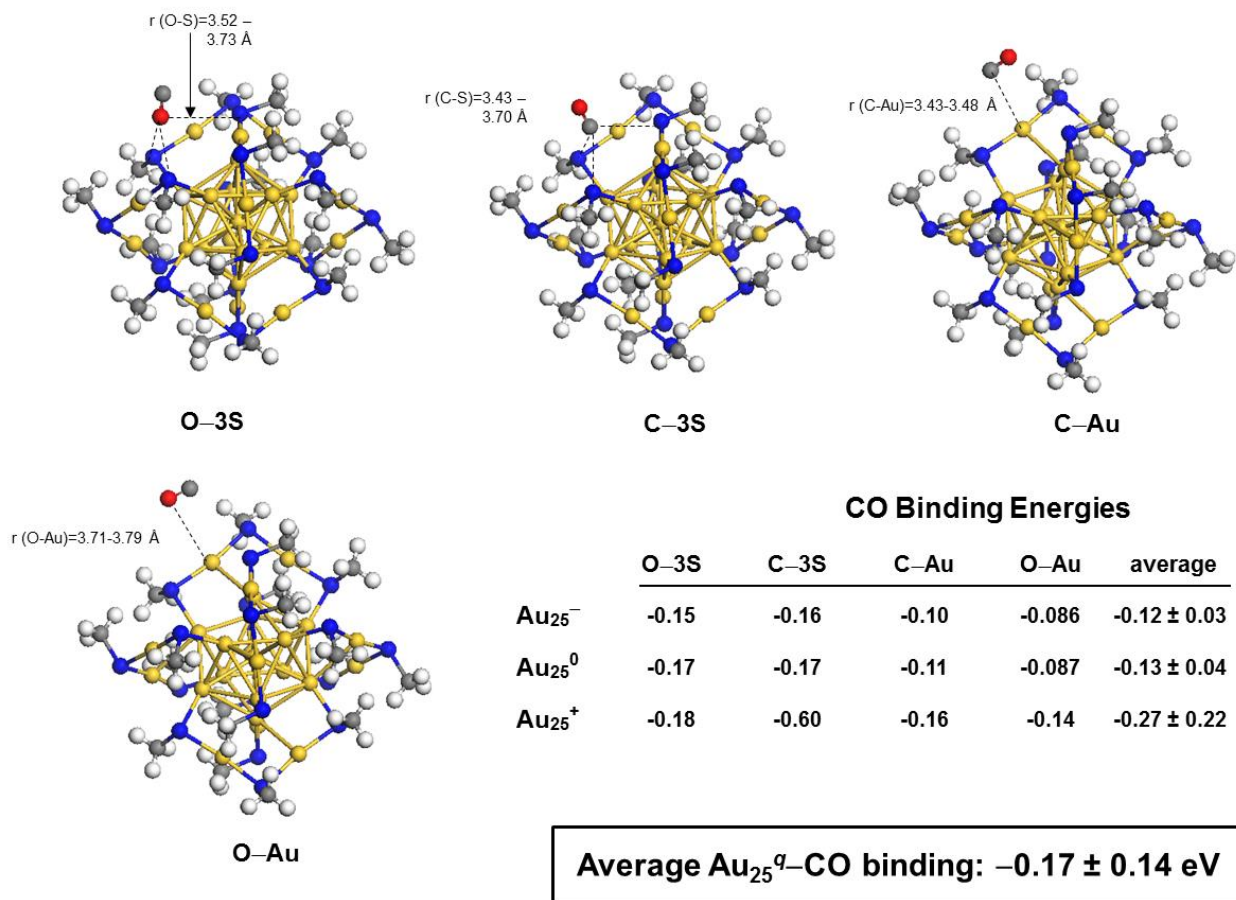


**Figure S14.** Ball-and-stick representations and binding energies of the singly-bound  $\text{Au}_{25}^q$ -CO system. Atom colors: Au: gold, S: blue, C: grey, H: white, O: red.

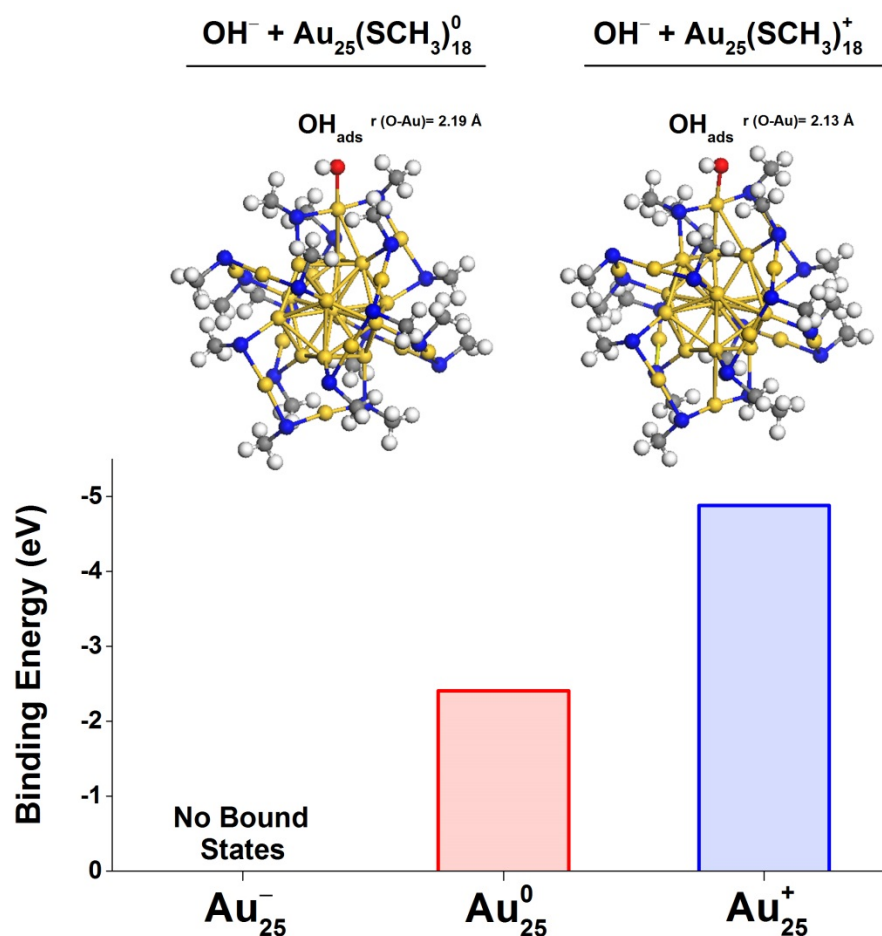


**Figure S15.** Calculated binding energies and DFT models of OH<sup>-</sup> adsorption at Au<sub>25</sub>(CH<sub>3</sub>)<sub>18</sub><sup>q</sup> clusters ( $q = -1, 0, +1$ ).

Cluster models were based on the published Au<sub>25</sub><sup>-</sup> crystal structure<sup>1</sup> and a previously DFT-optimized model.<sup>10</sup> OH<sup>-</sup> binding energies are listed in table S1. These DFT results support the experimentally observed trend of stronger OH binding at Au<sub>25</sub><sup>+</sup> (table S2).

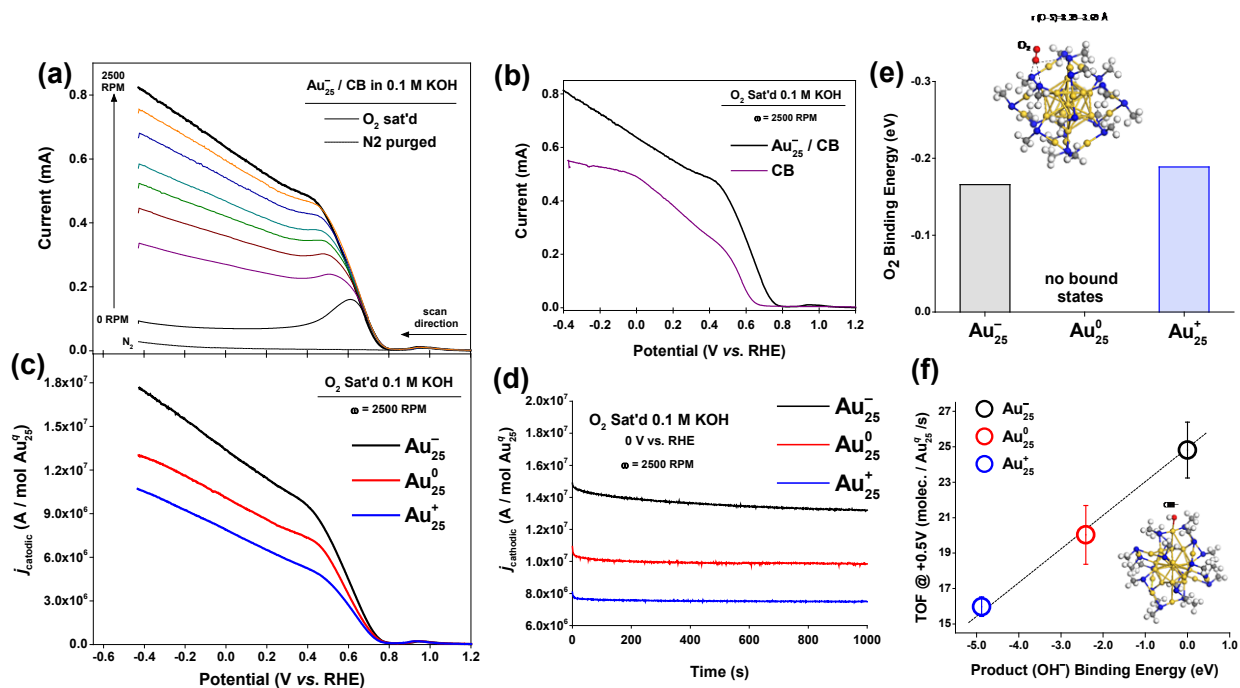


**Figure S16.** (a) RDE voltammograms of  $\text{Au}_{25}^-$  in  $\text{N}_2$  purged and  $\text{O}_2$  saturated 0.1M KOH at various rotation rates. (b) Comparison of  $\text{O}_2$  reduction at the catalyst-free CB support and CB-supported  $\text{Au}_{25}^-$ . (c) Polarization curves of the  $\text{Au}_{25}^q$  charge states in  $\text{O}_2$  saturated 0.1M KOH;  $\omega = 2500$  RPM. (d) RDE electrolysis at 0.0 V in  $\text{O}_2$  saturated 0.1M KOH ( $\omega = 2500$  RPM). (e) DFT-predicted  $\text{O}_2$ - $\text{Au}_{25}^q$  binding energies and representative model. (f) Correlation between experimentally determined ORR TOF at +0.5 V and the binding energy of the ORR reaction product ( $\text{OH}^-$ ). A representative  $\text{Au}_{25}^+-\text{OH}$  model is also presented.

## $\text{O}_2$ Reduction Reaction (in alkaline electrolyte)

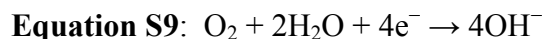


Figure S16a shows RDE polarization curves at different rotation rates in  $\text{O}_2$  saturated 0.1M KOH. The differently charged  $\text{Au}_{25}^q$  clusters demonstrated equivalent ORR electron transfer numbers of  $n = 3.0 \pm 0.3 e^-$  between +0.5V and -0.35V vs. RHE (triplicate runs for each  $\text{Au}_{25}^q$  charge state). This indicates  $\text{Au}_{25}^q$  reduced  $\text{O}_2$  through a combination of  $2e^-$  and  $4e^-$  processes (Equations S9 and S10). In comparison, the CB support demonstrated an electron transfer number of  $n = 2.46 e^-$  and commercially available Pt-decorated CB (10% weight Pt; *Sigma Aldrich*) demonstrated an electron transfer number of  $n = 3.75 e^-$ . Electron transfer numbers were calculated using the Levich equation as described in figure S12 using the values  $C_{\text{O}_2} = 1.2 \times 10^{-6} \text{ mol/cm}^3$  and  $D_{\text{O}_2} = 1.9 \times 10^{-5} \text{ cm}^2/\text{s}$ .

Figure S16b compares O<sub>2</sub> reduction at CB-supported Au<sub>25</sub><sup>-</sup> and the catalyst-free CB support. The CB support also showed O<sub>2</sub> reduction activity, but the ORR onset at the catalyst free CB support was shifted by approximately -100 mV compared with the Au<sub>25</sub><sup>q</sup> clusters. Catalyst loadings were kept between 3.3–7.7x10<sup>-11</sup> mol Au<sub>25</sub><sup>q</sup>. No significant current density vs. catalyst loading trends were observed in this loading regime.

Polarization and electrolysis data show an ORR activity trend of Au<sub>25</sub><sup>-</sup> > Au<sub>25</sub><sup>0</sup> > Au<sub>25</sub><sup>+</sup> (Figures S16c-d and Table 1 in the main text). The retention of charge state-dependent O<sub>2</sub> activity indicates during constant potential electrolysis indicates the Au<sub>25</sub><sup>q</sup> charge state influence reactivity over extended periods of time. O<sub>2</sub> is reduced into OH<sup>-</sup> and OOH<sup>-</sup> in alkaline electrolytes. DFT identified weak spontaneous binding between Au<sub>25</sub><sup>q</sup> and O<sub>2</sub> (Figure S16e), which confirms the need for electrochemical potentials during the ORR and previous analysis of O<sub>2</sub> adsorption at ground-state Au<sub>25</sub><sup>q</sup> clusters.<sup>2, 14</sup> On the other hand, experimental and computational results show stronger OH binding at the positively charged Au<sub>25</sub><sup>+</sup> cluster (Tables S1, S2 and figure S15). Figure S16f correlates the ORR TOF at +0.5V and the reaction product (OH<sup>-</sup>) binding energy. We chose to present TOF at +0.5V because the contribution from the CB support is small at this potential, although Au<sub>25</sub><sup>-</sup> showed significantly higher ORR TOFs (>95% CL) at all potentials between +0.5 V and -0.4V. In this case, the positively charged Au<sub>25</sub><sup>+</sup> binds the ORR products more strongly compared with the other clusters. This blocks the Au<sub>25</sub><sup>+</sup> surface and reduces its ORR activity. Strong OH<sup>-</sup> adsorption is also known to block the active sites of other ORR catalysts.<sup>24</sup> While we only specifically analyzed OH<sup>-</sup> binding, we also expect an equivalent binding energy trend for the negatively charged OOH<sup>-</sup> reaction product.

We can compare our ORR results to previously published studies. For example, Chen and Chen investigated the ORR activity of unsupported Au<sub>25</sub><sup>-</sup> clusters deposited directly onto GC electrodes.<sup>25</sup> They reported an electron transfer number of n = 4.06 e<sup>-</sup> and a current density of 10 mA cm<sup>-2</sup><sub>Au</sub> at 0.4 V vs. RHE. Based on our calibration of Au<sub>25</sub><sup>q</sup> loading in figure S5: 10 mA/cm<sup>2</sup><sub>Au</sub> converts into [(10 mA/cm<sup>2</sup><sub>Au</sub>)(1A/1000 mA)(1 cm<sup>2</sup><sub>Au</sub>/390x10<sup>-6</sup> C)(356865 C/mol Au<sub>25</sub><sup>q</sup>) = 9.2x10<sup>6</sup> A/mol Au<sub>25</sub><sup>q</sup>. Their value is in excellent agreement with our measured ORR current density of 9.5x10<sup>6</sup> A/mol Au<sub>25</sub><sup>-</sup> at 0.4 V vs. RHE (Figure S16c). The value for bulk Au electrochemical surface area (390x10<sup>-6</sup> C/cm<sup>2</sup><sub>Au</sub>) was taken from reference <sup>5</sup>.

**Table S1.** Comparison of singly adsorbed and coadsorbed reactant binding at  $\text{Au}_{25}^q$ ; all values are eV.

	Singly Adsorbed Reactants			Coadsorbed	Singly Adsorbed Reactants			Coadsorbed
	$\text{H}^+$	$\text{CO}_2$	sum	$\text{CO}_2 + \text{H}^+$	$\text{OH}^-$	$\text{CO}$	sum	$\text{CO} + \text{OH}^-$
$\text{Au}_{25}^-$	-12.20	$-0.13 \pm 0.02$	$-12.33 \pm 0.02$	$-12.25 \pm 0.02$	0.0	$-0.12 \pm 0.03$	$-0.12 \pm 0.03$	-0.01
$\text{Au}_{25}^0$	-9.44	$-0.13 \pm 0.04$	$-9.57 \pm 0.04$	$-10.03 \pm 0.07$	-2.41	$-0.13 \pm 0.04$	$-2.54 \pm 0.04$	$-2.38 \pm 0.05$
$\text{Au}_{25}^+$	-8.21	$-0.29 \pm 0.28$	$-8.50 \pm 0.28$	$-8.06 \pm 0.23$	-4.88	$-0.27 \pm 0.22$	$-5.15 \pm 0.22$	$-4.76 \pm 0.13$

**Table S2.** OH stripping potentials from  $\text{Au}_{25}^q$  in 0.1M KOH. Potentials are referenced versus the reversible hydrogen electrode (RHE).

	<b>0.1 M KOH</b> (50 mV/s)	<b>0.1M KHCO<sub>3</sub></b> (10 mV/s)
$\text{Au}_{25}^-$	$0.978 \pm 0.010$ (n = 22)	$1.052 \pm 0.021$ (n = 15)
$\text{Au}_{25}^0$	$0.969 \pm 0.008$ (n = 19)	$1.015 \pm 0.034$ (n = 9)
$\text{Au}_{25}^+$	$0.968 \pm 0.009$ (n = 21)	$0.996 \pm 0.042$ (n = 12)

OH stripping from  $\text{Au}_{25}^+$  occurred at more negative potentials compared with  $\text{Au}_{25}^-$ . While the potential differences are somewhat small, the differences between  $\text{Au}_{25}^+$  and  $\text{Au}_{25}^-$  are significant at a confidence level greater than 99%. These experimental results are qualitatively consistent with our DFT prediction of stronger  $\text{OH}^-$  binding at the positively charged  $\text{Au}_{25}^+$  cluster (Table S1 and figure S15).

## Supporting Information References

1. (a) M. Zhu, C. M. Aikens, F. J. Hollander, G. C. Schatz and R. Jin, *J. Am. Chem. Soc.*, 2008, **130**, 5883-5885; (b) M. W. Heaven, A. Dass, P. S. White, K. M. Holt and R. W. Murray, *J. Am. Chem. Soc.*, 2008, **130**, 3754-3755.
2. D. R. Kauffman, D. Alfonso, C. Matranga, G. Li and R. Jin, *J. Phys. Chem. Lett.*, 2013, **4**, 195-202.
3. (a) P. Rodriguez, N. Garcia-Araez and M. T. M. Koper, *Phys. Chem. Chem. Phys.*, 2010, **12**, 9373-9380; (b) P. Rodríguez, A. A. Koverga and M. T. M. Koper, *Angew. Chem. Int. Ed.*, 2010, **49**, 1241-1243.
4. Y. Negishi, K. Nobusada and T. Tsukuda, *J. Am. Chem. Soc.*, 2005, **127**, 5261-5270.
5. S. Trasatti and O. A. Petrii, *Pure & Appl. Chem.*, 1991, **63**, 711-734.
6. T. F. Jaramillo, K. P. Jørgensen, J. Bonde, J. H. Nielsen, S. Horch and I. Chorkendorff, *Science*, 2007, **317**, 100-102.
7. (a) G. Kresse and J. Furthmüller, *Phys. Rev. B*, 1996, **54**, 11169-11186; (b) J. Hafner, *J. Comp. Chem.*, 2008, **29**, 2044-2078.
8. J. P. Perdew, K. Burke and Y. Wang, *Phys. Rev. B*, 1996, **54**, 16533-16539.
9. G. Kresse and D. Joubert, *Phys. Rev. B*, 1999, **59**, 1758-1775.
10. C. M. Aikens, *J. Phys. Chem. C*, 2008, **112**, 19797-19800.
11. D. R. Kauffman, D. Alfonso, C. Matranga, H. Qian and R. Jin, *J. Am. Chem. Soc.*, 2012, **134**, 10237-10243.
12. K. Kwak and D. Lee, *J. Phys. Chem. Lett.*, 2012, **3**, 2476-2481.
13. D. Lee, R. L. Donkers, G. Wang, A. S. Harper and R. W. Murray, *J. Am. Chem. Soc.*, 2004, **126**, 6193-6199.
14. O. Lopez-Acevedo, K. A. Kacprzak, J. Akola and H. Häkkinen, *Nature Chem.*, 2010, **2**, 329-334.
15. (a) M. Watanabe, H. Sei and P. Stonehart, *J. Electroanal. Chem.*, 1989, **261**, 375-387; (b) I. Streeter, R. Baron and R. G. Compton, *J. Phys. Chem. C*, 2007, **111**, 17008-17014; (c) Y. E. Seidel, A. Schneider, Z. Jusys, B. Wickman, B. Kasemob and R. J. Behm, *Faraday Discuss.*, 2008, **140**, 167-184; (d) S. E. F. Kleijn, S. C. S. Lai, M. T. M. Koper and P. R. Unwin, *Angew. Chem. Int. Ed.*, 2014, **53**, 3558-3586.
16. M. Zhu, W. T. Eckenhoff, T. Pintauer and R. Jin, *J. Phys. Chem. C*, 2008, **112**, 14221-14224.
17. (a) Y. Negishi, M. Mizuno, M. Hirayama, M. Omatoi, T. Takayama, A. Iwase and A. Kudo, *Nanoscale*, 2013, **5**, 7188-7192; (b) Y. Liu, H. Tsunoyama, T. Akita and T. Tsukuda, *Chem. Commun.*, 2010, **46**, 550-552.
18. E. S. Shibu, M. A. Habeeb Muhammed, T. Tsukuda and T. Pradeep, *J. Phys. Chem. B*, 2008, **112**, 12168-12176.
19. Y. Chen and M. W. Kanan, *J. Am. Chem. Soc.*, 2012, **134**, 1986-1989.
20. A. J. Bard and L. R. Faulkner, *Electrochemical Methods: Fundamentals and Applications*, 2nd ed., John Wiley & Sons, New York, 2001.
21. B. B. Blizanac, C. A. Lucas, M. E. Gallagher, M. Arenz, P. N. Ross and N. M. Marković, *J. Phys. Chem. B*, 2004, **108**, 625-634.
22. B. E. Hayden, *Acc. Chem. Res.*, 2013, **46**, 1858-1866.
23. S. Wang, D. Yu and L. Dai, *J. Am. Chem. Soc.*, 2011, **133**, 5182-5185.

24. (a) N. M. Marković, T. J. Schmidt, V. Stamenković and P. N. Ross, *Fuel Cells*, 2001, **1**, 105-116; (b) D. Wang, H. L. Xin, Y. Yu, H. Wang, E. Rus, D. A. Muller and H. D. Abruña, *J. Am. Chem. Soc.*, 2010, **132**, 17664-17666.
25. W. Chen and S. Chen, *Angew. Chem. Int. Ed.*, 2009, **48**, 4386-4389.